THERMO-ELECTROKINETIC ROTATING NON-NEWTONIAN HYBRID NANOFLUID FLOW FROM AN ACCELERATING VERTICAL SURFACE

[1]J. Prakash, [*2]Dharmendra Tripathi, [3]O. Anwar Bég, [4]AK Tiwari and **[5]Rakesh Kumar**

[1]*Department of Mathematics, Avvaiyar Government College for Women, Karaikal – 609 602, U.T of Puducherry, **India.***

[2]*Department of Mathematics, National Institute of Technology, Uttarakhand, Srinagar– 246174, **India**.*

[3]*Multi-PhysicalEngineering Sciences Group, Dept. Mechanical/Aeronautical Engineering, Salford University, Manchester, M54WT, **UK**.*

[4]*Department of Applied Mechanics, Motilal Nehru National Institute of Technology Allahabad, Prayagraj, Uttar Pradesh 211004, India.*

[5]*Department of Mechanical Engineering, Manipal University Jaipur, Jaipur, Rajasthan 303007, India.*

Corresponding author: dtripathi@nituk.ac.in

ABSTRACT:

This paper explores the combined effects of Coriolis force and electric force on the rotating boundary layer flow and heat transfer in a viscoplastic hybrid nanofluid from a vertical exponentially accelerated plate. The hybrid nanofluid comprises two different types of metallic nanoparticles, namely silver (*Ag*) and magnesium oxide (*MgO*) suspended in an aqueous base fluid. The Casson model is deployed for non-Newtonian effects. An empirical model is implemented to determine the thermal conductivity of the hybrid nanofluid. Rosseland's radiative diffusion flux model is also utilized. Axial electrical field is considered and the Poisson-Boltzmann equation is linearized via the Debye-Hückel approach. The resulting coupled differential equations subject to prescribed boundary conditions are solved with Laplace transforms. Numerical evaluation of solutions is achieved via MATLAB symbolic software. A parametric study of the impact of key parameters on axial velocity, transverse velocity, nanoparticle temperature and Nusselt number is conducted for both hybrid (Ag-MgO)-water nanofluid and also unitary (Ag)-

water nanofluid. With increasing volume fraction of silver nanoparticles there is a reduction in both axial velocity and temperatures whereas there is a distinct elevation in transverse velocity for both unitary and hybrid nanofluid. Elevation in heat absorption parameter strongly decreases axial velocity whereas it enhances transverse velocity. Increasing radiation parameter strongly boosts temperatures. Increasing heat absorption parameter significantly accelerates the transverse flow. Negative values of Helmholtz-Smoluchowski velocity decelerate the axial flow whereas positive values accelerate it; the opposite behavior is observed for transverse velocity. Increasing Taylor number significantly damps both the axial (primary) and transversal (secondary) flow. Increasing thermal Grashof number strongly enhances the axial flow but damps the transverse flow. Unitary nanofluid achieves higher Nusselt numbers than hybrid nanofluid but these are decreased with greater radiative effect (since greater heat transport away from the plate surface), Prandtl number and heat absorption. Nusselt number is significantly reduced with greater time progression and values are consistently higher for unitary nanofluid compared with hybrid nanofluid. The computations provide insight into more complex electrokinetic rheological nanoscale flows of relevance to biomedical rotary electro-osmotic separation devices.

KEYWORDS: *Casson Rheological Model; Hybrid Nanofluids; Rotating Electroosmotic Flow; Radiative Flux; Taylor Number; Heat Transfer.*

1. INTRODUCTION

Heat transfer with boundary layer flow through an accelerated surfaceis a fundamental area of fluid dynamics arising in a diverse spectrum of technological applications. Vertical surfaces arise in for example coating dynamics, surface treatment, spray deposition, biological sterilization, electro-microfluidics, polymer stretching etc. Such areas frequently feature multiple physical phenomena e.g. electrical fields, radiative heat transfer, thermo-capillary convection, non-Newtonian behaviour etc. In relation to the forced movements brought by surface forces, the motion of the fluid is generally considered to be a natural flow due to the action of the gravitational field. Thermal buoyancy effects are therefore critical to such viscous flows when heat is present. On the other hand, the free convection term is negated when natural convection flow is not considered at the finite bounded area. Stokes first studied the flow of an incompressible viscous liquid from an impulsively initiated infinite vertical plate surface and this important hydrodynamic

problem was revisited later by Rayleigh [1]. Pohlhausen [2] extended this study to consider heat transfer, specifically when the plate and the ambient fluid are maintained at constant but different temperatures, and presented analytical series solutions for this velocity stream and temperature distribution for a Prandtl number of 0.733 (air). Schuh [3] generalized Pohlhausen's study to consider higher Prandtl numbers of up to 1000 which are representative of highly viscous fluids e.g. polymers. A rigorous experimental and theoretical investigation was presented by Schmidt and Beckmann [4] who focused on the free convection in air by means of the gravitational force in boundary layer transport from a vertical flat plate [4]. A comprehensive analysis of the problem was made by Ostrach [5] who produced numerical solutions obtained for several values of Prandtl number, noting the importance of properly representing three major physical quantities i.e. the coefficient of fluid-volumetric expansion, the body force and temperature variation. Subsequently free convection from vertical surfaces has stimulated considerable interest in engineering sciences owing to emerging applications in nuclear reactor systems, materials processing, thermal barrier coating design, geophysics, solar collectors and more recently biomedical devices. Soundalgekar [6] studied free convection flow along a vertical surface when cooled or heated by free convection currents. Yang et al. [7] employed a finite difference computational procedure to simulate the laminar convection from vertical plates with periodically changing surface temperature, for a wide range of oscillation frequencies and large amplitudes. In recent years many diverse studies of natural convection from vertical surfaces have been communicated addressing a range of complex effects including variable viscosity magnetic nanofluids [8], convective-radiative heating in Williamson rheological flows [9], thermophysical second grade viscoelastic flows [10], entropy generation in transient secondar-grade Reiner Rivlin differential fluids [11] and cross diffusion effects in permeable media [12]. In boundary layer theory, the boundary velocity and thermal conditions are very significant to analyze. The convection boundary conditions define the presence of convection (heating or cooling) at the walls which are applicable in various thermal systems. Some of the mathematical models on thermal effects which have been developed include metabolic structure in physiological systems [13], entropy generation during the blood flow [14], three-dimensional couple stress fluid flow [15] and magnetohydrodynamics with power law fluids [16].

Building on the initial success achieved with nanofluids [17], which are colloidal suspensions of metallic/non-metallic nanoparticles in base fluids (e.g. water) aimed at achieving thermal enhancement, more recently engineers have explored combining different nano-particls in a single

nanofluid. These constitute hybrid nanofluids and judicious selection of different metallic nanoparticles e.g. copper, silver, gold, magnesium, zinc etc have shown yet further improvements in thermal conductivity properties. Hybrid nanofluids may generally include those prepared with multiple types (2 or more nanoparticles) suspended in a single base liquid *or* single nanoparticles with different base liquid combinations e.g. water, ethylene glycol etc. A hybrid material is a substance which combines the chemical and physical characteristics of various materials in a homogeneous and stable manner. Inspection of the literature shows that the hybrid nanomaterials exhibit physicochemical characteristics that do not occur in the individual components. Significant applications of hybrid nanomaterials are emerging and include electrochemical sensors, biosensors, nanocatalysts [18-19] and composite materials composed of carbon nanotubes (CNTs). However, hybrid nanofluids have yet to be more extensively explored in emerging applications deploying hybrid nanomaterials. Relatively sparse work has been communicated on numerical and laboratory studies of hybrid nanofluid transport. However some interesting recent scientific works have appeared. Jana *et al.* [20] investigated hybrid combinations of carbon nanotubes (CNTs), copper nanoparticles (CuNPs) and gold nanoparticles (AuNPs), noting that unitary nanofluids outperform hybrid nanofluids for thermal conductivity enhancement and furthermore higher thermal conductivities are achieved than those predicted by theory. They further showed that CNTs in nanofluid CuNP also decreased sedimentation effects. Turcu *et al.* [21] described the synthesis of conducting polypyrrole (PPY) and multi wall carbon nanotubes (MWCNTs) combined with Fe_3O_4 aqueous nanofluid (using spray pyrolysis and oxidation polymerization) to generate a novel hybrid nanostructure of MWCNTs coated with PPY containing magnetic nanoparticles. Hybrid nanofluids may therefore feature both multiple metallic nanoparticles and/or carbon-based nanoparticles to produce modifications in thermal properties [22, 23]. Baghbanzadeha *et al.* [24] synthesized the hybrid of silica nanosphere/multiwall carbon nanotube (MWCNT) and reported that thermal conductivity of the fluids were associated with MWCNTs (23.3%) and silica nanospheres (8.8%). Devi and Devi [25, 26] studied both two-dimensional and three-dimensional stretching sheet flows of hybrid $Cu-Al_2O_3$ /water nanofluids, observing that higher volume fractions of nanoparticles' volume enhance heat transfer. Hayat and Nadeem [27] studied the effects of radiative heat transfer and chemical reaction on rotating stretching sheet flow of Ag–CuO/water hybrid nanofluids. Lund *et al.* [28] used Runge-Kutta quadrature to analyze the boundary layer flow of dissipative $Cu–Fe_3O_4/H_2O$ hybrid nanofluids from a nonlinear

expanding/contracting sheet in a porous medium. Very recently Tripathi *et al.* [29] used FREEFEM++ finite element software to compute the unsteady viscous pharmaco-dynamics in a stenotic diseased artery with hybrid biocompatible nanoparticles (Silver and Gold) and a Tiwari-Das model. Other computational hybrid nanofluid dynamics studies have addressed Cu-Al_2O_3/H_2O nanofluids [30], $SiO_2-Al_2O_3$/water hybrid nanofluids in curved surface stagnation flows [31], hybrid MoS_2/SiO_2 nanofluids [32], magnetohydrodynamic hybrid Cu-Al_2O_3/water nanofluid flows from radially stretching/shrinking surfaces [33], SWCNT-MgO hybrid nanofluids [34], Ag–MgO hybrid nanofluids in cavity regions [35]. A detailed appraisal of both the beneficial and detrimental aspects of hybrid nanofluids has been presented by Sundar *et al*. [36] including an emphasis on how heat transfer, friction factor and Nusselt number may or may not be enhanced with hybrid nanoparticle combinations depending on the specific application considered.

The above studies have generally neglected electrical field effects in aqueous unitary or hybrid nanofluids. The ions in ionic aqueous nanofluids are stimulated when an electric field is applied. When the ions move, the nanofluid is dragged and this creates a macroscopic flow which is known as *electroosmotic flow.* Electroosmotic flow is a transport mechanism frequently encountered in nature [37] which can be artificially produced in various technologies. It is significantly different from conventional viscous laminar flow since the driving force is the externally applied electrical field, not a pressure gradient. At the microscale in channels and near boundaries, the electrostatic body force produces an excess of positively charged anions in the Debye electrical double layer close to the boundary. These excess charges in the double layer are attracted under an electric potential by electrostatic forces, and therefore migrate towards negative electrodes (cations). This intimate viscous coupling results in the pumping of the bulk liquid by the mobile layer [38]. Electro-osmotic flow can therefore be exploited in many complex ionic hydrodynamic systems. In chemical separation techniques, electroosmotic flow is an important component, especially capillary electrophoresis. Electroosmosis flow also features in soil studies [39] and microfluidic devices with heavily charged surfaces (often oxides) which are regularly active [40]. It is also a critical feature in emerging biomedical technologies such as polyelectrolyte grafted rotating narrow fluidic channels and surfaces in medicine [41] wherein the rotational force-driven ionic flow can be effectively modulated by the soft layer induced alteration in the electrostatic potential under electrokinetic actuation. Other applications include biochemical mixing processes and nanofluidics [42]. A number of analytical and computational studies of electro-osmotic flows have

been produced in recent years. Jian *et al.* [43] have developed analytical solutions for the oscillatory electroosmotic flow of Maxwell viscoelastic fluids in rectangular microchannels. Ali *et al.* [44] investigated theoretically the electro-osmotic pumping in two-fluid (inner core of Ellis rheological fluid and peripheral Newtonian layer) flow through a cylindrical tube with electro-kinetic wall slip. Narla *et al.* [45] computed the non-Newtonian electroosmotic peristaltic dynamics in a deformable tube with applications in fertility treatment. Tripathi *et al.* [46] derived analytical solutions for electroosmotic peristaltic transport in a bio-inspired conduit containing a Darcian isotropic porous medium. Tripathi *et al.* [47] theoretically investigated the electrokinetic propulsion of Stokes' couple stress aqueous ionic biofluids in a deformed microchannel under axial electrical field. Many other interesting configurations have been explored in the field of electroosmotic fluid mechanics [48-55] which have addressed multiple phenomena including slip effects, simultaneous magnetic field action, Joule heating and nanoscale behaviour (nanofluids).

Inspection of the literature has revealed that thus far very little attention has been directed at the performance of hybrid nanofluids in rotating electro-osmotic flows. Coriolis effects have been considered for other types of fluids e.g. third grade viscoelastic fluids [56] and power-law (shear thinning/thickening fluids) [57]. However Casson viscoplastic hybrid nanofluids rotating electro-osmotic flows have yet to be considered. The present study aims to extend the current literature to consider the collective effects of radiative transfer, heat absorption, thermal buoyancy, Coriolis force and electrical body force on the rotating viscoplastic (Casson) boundary layer flow and heat transfer in a viscoplastic hybrid nanofluid from a vertical exponentially accelerated plate. The hybrid nanofluid comprises two different types of metallic nanoparticles, namely silver (Ag) and magnesium oxide (*MgO*) suspended in an aqueous base fluid. A Maxwell-Garnett model is implemented to determine the thermal conductivity of the hybrid nanofluid. Rosseland's radiative diffusion flux model is also utilized. Silver nanoparticles are known to be anti-bacterial agents and offer significant advantages in biomedical devices. The relative performance of hybrid Ag–MgO/water nanofluid to unitary Ag/water nanofluid is assessed. Analytical solutions for the linearized conservation equations are presented by virtue of carefully selected boundary conditions. MATLAB software is used to evaluate the solutions for the influence of key parameters including volume fraction of silver nanoparticles, heat absorption parameter, radiation parameter, Helmholtz-Smoluchowski velocity, Taylor number, thermal Grashof number and inverse Debye length parameter on axial (primary) and transverse (secondary) velocity, temperature and Nusselt

number at the plate surface are visualized graphically and interpreted at length. The simulations provide a good benchmark for further computational fluid dynamics studies of relevance to rotational biochemical electro-kinetic mixing and separation devices [58].

2. MATHEMATICAL MODEL

2.1. Problem definition

Fig. 1 shows the regime under investigation. An $(\bar{X}, \bar{Y})$ coordinate system is adopted. Electroosmotic flow of an incompressible hybrid Casson Ag–MgO/water nanofluid is considered adjacent to an exponentially accelerated plate. The plate lies in the $\bar{X} - \bar{Y}$ plane. A uniform electrical field, $E_{\bar{X}}$ is applied in the $\bar{X}$-direction. A volumetric rate of heat absorption is present and a uniform radiative flux acts in the $\bar{Y}$-direction. When $\bar{t} \leq 0$, the fluid and plate are at static and preserved in the uniform temperature T_∞. For $\bar{t} > 0$ the plate starts accelerating in the $\bar{X}$direction with time-dependent velocity $u_0 \cos(\bar{\varpi}\bar{t})$. The whole system (plate and ionic nanofluid) rotates in unison about the $\bar{Y}$ -axis with uniform angular velocity, $\bar{\varpi}$. The base liquid and the suspended nanoparticles are in thermal equilibrium. The following assumptions are used in the present analysis:

(i) All other basic fluid characteristics are constant and the fluid follows the Boussinesq approximation.

(ii) The Poisson-Boltzmann equation is linearized via the Debye-Hückel approach.

(iii) The thermophysical characteristics of hybrid nanofluids are assumed to be functions of particle volume fraction (see Table 1)

(iv) The fluid flow is transient and laminar in nature.

(v) The radiation heat flux in the direction of the plate is minimal as compared to the normal direction.

(vi) The impacts of viscous dissipation, Ohmic dissipation and induced magnetic field are not considered.

(vii) Chemical reaction is not considered.

2.2. Casson hybrid nanofluid and thermo-physical properties

The rheological characteristics are simulated with the Cauchy stress tensor for a Casson yield stress (viscoplastic) fluid which is defined following [59]:
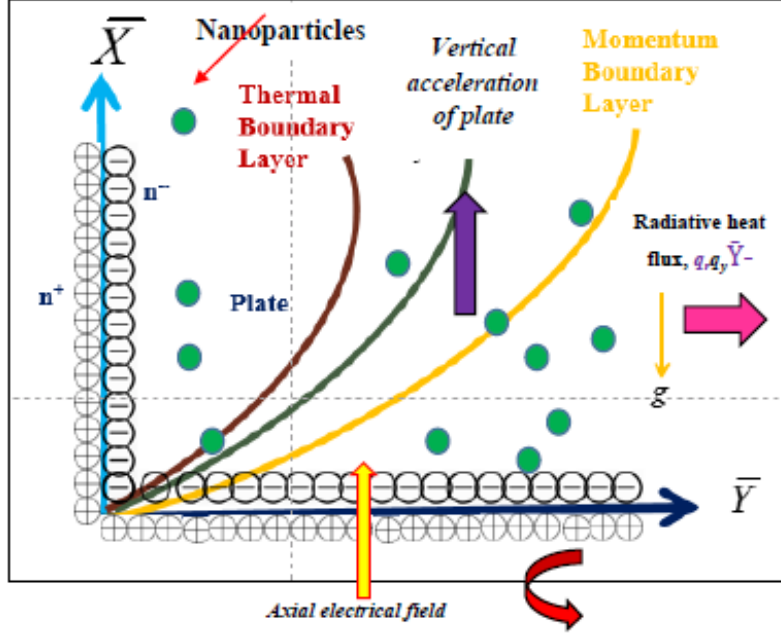
Fig. 1 Flow geometry for rotating electro-osmotic hybrid nanofluid flow from accelerating plate

$$\tau_{ij} = 2\,e_{ij}\left(\frac{P_{\bar{Y}}}{\sqrt{2\pi}} + \mu_{hnf}\right) \qquad if \quad \pi \geq \pi_C, \tag{1}$$

$$\tau_{ij} = 2\,e_{ij}\left(\frac{P_{\bar{Y}}}{\sqrt{2\pi}_C} + \mu_{hnf}\right) \qquad if \quad \pi < \pi_C. \tag{2}$$

Here $P_{\bar{Y}}$ is the Casson yield stress defined as:

$$P_{\bar{Y}} = \frac{\mu_{hnf}\sqrt{2\pi}}{\gamma}, \tag{3}$$

Here π, μ_{hnf}, π_c are the product of the component of deformation rate, the plastic dynamic viscosity of the hybrid nanofluid and a critical value respectively. It is also noteworthy that $\pi = e_{ij}e_{ij}$ and e_{ij} is the $(i,j)^{th}$ element of the deformation rate. For the hybrid Casson (viscoplastic) nanofluid, where $\pi < \pi_C$, it can be assumed that:

$$\mu = \frac{P_{\bar{Y}}}{\sqrt{2\pi}} + \mu_{hnf}. \tag{4}$$

Inserting Eqn. (3) into (4), the kinematic viscosity of hybrid Casson nanoliquid can be shown to depend on plastic dynamic viscosity μ_{hnf}, density of hybrid nanofluid ρ_{hnf} and Casson parameter γ, as follows:

$$\mathcal{G} = \left(1 + \frac{1}{\gamma}\right)\frac{\mu_{hnf}}{\rho_{hnf}}. \tag{5}$$

The momentum and energy conservation equations for the rotating thermo-electroosmotic flow of hybrid Casson nanofluid may be shown to take the following form, based on an amalgamation of the models appearing in [55-57, 59, 64]:

$$\rho_{hnf}\frac{\partial \bar{U}}{\partial \bar{t}} = \mu_{hnf}\left(1+\frac{1}{\gamma}\right)\frac{\partial^2 \bar{U}}{\partial \bar{Y}^2} + 2\rho_{hnf}\Omega\bar{V} + \rho_e\bar{\Phi}_{\bar{X}} + g\,(\rho\beta)_{hnf}\,(\bar{T}-T_\infty), \tag{6}$$

$$\rho_{hnf}\frac{\partial \bar{V}}{\partial \bar{t}} = \mu_{hnf}\left(1+\frac{1}{\gamma}\right)\frac{\partial^2 \bar{V}}{\partial \bar{Y}^2} - 2\rho_{hnf}\Omega\bar{U} + g\,(\rho\beta)_{hnf}\,(\bar{T}-T_\infty), \tag{7}$$

$$(\rho c_p)_{hnf}\frac{\partial \bar{T}}{\partial \bar{t}} = \kappa_{hnf}\frac{\partial^2 \bar{T}}{\partial \bar{Y}^2} - Q_0(\bar{T}-T_\infty) - \frac{\partial \bar{q}_r}{\partial \bar{Y}}. \tag{8}$$

In Eqns. (6)-(8) $\bar{U}$ and $\bar{V}$ represent the velocity components in axial and transverse direction respectively, Ω, g, $(\rho\beta)_{hnf}$, $(\rho c_p)_{hnf}$, κ_{hnf}, Q_0 and $\bar{q}_r$ are the angular velocity, acceleration due to gravity, thermal expansion coefficient of hybird nanofluid, heat capacitance of the hybrid nanofluid, thermal conductivity of hybrid nanofluid, variable volumetric heat generation (or absorption) rate and radiative heat flux. Also, $\bar{\Phi}_{\bar{X}}$ is the electric body force termand ρ_e is the net charge number density. In this analysis, the dynamic viscosity of the hybrid nanofluid μ_{hnf} and thermal conductivity of the hybrid nanofluid κ_{hnf} are evaluated with new empirical correlations suggested by Esfe *et al.* [60], which are precisely formulated for Ag–MgO/water hybrid nanofluid:

$$\mu_{hnf} = \mu_{bf}\left(1 + 32.795\phi_{hnf} - 7214\phi_{hnf}^2 + 714600\phi_{hnf}^3 - 0.1941\times10^8\,\phi_{hnf}^4\right),\ 0 \le \phi_{hnf} \le 0.02 \tag{9}$$

$$\kappa_{hnf} = \frac{\kappa_{bf}\left(0.1747\times10^5 + \phi_{hnf}\right)}{0.1747\times10^5 - 0.1498\times10^6\,\phi_{hnf} + 0.1117\times10^7\,\phi^2_{hnf} + 0.1997\times10^8\,\phi^3_{hnf}}, \quad 0 \le \phi_{hnf} \le 0.03 \quad (10)$$

The hybrid nanofluid of density ρ_{hnf}, the coefficient thermal expansion $(\rho\beta)_{hnf}$ and specific heat $(\rho c_p)_{hnf}$ are computed with the following mixtures rules [61, 62]:

$$\rho_{hnf} = \rho_{bf}\left[\left(1-\phi_{hnf}\right) + \frac{\phi_{Ag}\rho_{Ag} + \phi_{MgO}\rho_{MgO}}{\rho_{bf}}\right], \qquad (11)$$

$$(\rho\beta)_{hnf} = (\rho\beta)_{bf}\left[\left(1-\phi_{hnf}\right) + \frac{\phi_{MgO}(\rho\beta)_{MgO} + \phi_{Ag}(\rho\beta)_{Ag}}{(\rho\beta)_{bf}}\right], \qquad (12)$$

$$(\rho c_p)_{hnf} = (\rho c_p)_{bf}\left[\left(1-\phi_{hnf}\right) + \frac{\phi_{MgO}(\rho c_p)_{MgO} + \phi_{Ag}(\rho c_p)_{Ag}}{(\rho c_p)_{bf}}\right], \qquad (13)$$

Here volume fraction of the hybrid nanofluid i.e. $\phi_{hnf} = \phi_{Ag} + \phi_{MgO}$, is analyzed with an identical quantity of silver (Ag) and magnesium oxide (MgO) suspended in water (H_2O). Also, the subscript Ag specifies the properties of silver nanoparticles, subscript MgO represents the characteristics of magnesium oxide nanoparticles and subscript "bf" represents base fluid (water). **Table 1** gives the thermo-physical properties of nanoparticles and water-base fluid.

Table -1: Thermo-physical properties of (Ag-MgO / H₂O) hybrid nanofluid [61-63]

Physical properties	Ag	MgO	Pure water
Specific heat (c_p)($J/kg.K$)	235	955	4179
Density (ρ)(kg/m^3)	10500	3560	997.1
Thermal conductivity κ (W/mK)	429	45	0.623
Coefficient of thermal expansion $\beta X10^{-5}(K^{-1})$	1.89	1.13	1.67

2.3. Radiative heat flux

The local gradient for nanofluid may be expressed as follows [32, 55]:

$$\overline{q}_r = \frac{4\tilde{\sigma}}{3\tilde{k}} \frac{\partial \overline{T}^4}{\partial \overline{Y}},$$
(14)

where $\tilde{k}$ is Rosseland's mean absorption coefficient and the Stefan-Boltzmann constant is defined as $\tilde{\sigma}\,(=5.67 X 10^{-8}\, Wm^{-2}K^{-4})$.

If $\overline{T}^4$ is represented as a linear function of temperature then by extending $\overline{T}^4$ in a Taylor series around $\overline{T}_\infty$ and ignoring higher order components, we arrive at the formula

$$\overline{T}^4 \approx 4T_\infty^3 \overline{T} - 3T_\infty^4,$$
(15)

Substituting Eqns. (14) and (15) in (4), the energy Eqn. emerges as:

$$\frac{\partial \overline{T}}{\partial \overline{t}} = \frac{1}{(\rho c_p)_{hnf}} \left(\kappa_{hnf} + \frac{16\tilde{\sigma}T_\infty^3}{3\tilde{k}} \right) \frac{\partial^2 \overline{T}}{\partial \overline{Y}^2} - \frac{Q_0(\overline{T}-T_\infty)}{(\rho c_p)_{hnf}}.$$
(16)

Substituting equations (14) and (15) in (4), the energy Eqn. emerges as:

$$\frac{\partial \overline{T}}{\partial \overline{t}} = \frac{1}{(\rho c_p)_{hnf}} \left(\kappa_{hnf} + \frac{16\tilde{\sigma}T_\infty^3}{3\tilde{k}} \right) \frac{\partial^2 \overline{T}}{\partial \overline{Y}^2} - \frac{Q_0(\overline{T}-T_\infty)}{(\rho c_p)_{hnf}}.$$
(16)

2.4. Electroosmosis analysis

The Poisson equation defines the electrostatic potential produced in the ionicnanofluid by virtue of the creation of the electrical double layer:

$$\nabla^2 \overline{\Phi} = -\frac{\rho_e}{\varepsilon_{eff}},$$
(17)

Here $\varepsilon_{eff} = \varepsilon_0 \varepsilon_r$ where ε_0 specifies the relative permittivity of the vacuum and ε_r is the dielectric constant of the medium. For symmetric electrolyte solutions (ionic nanofluids), the charging number density is defined by assuming the same valence z in the cations and anions;

$$\rho_e = ez\left(n^+ - n^-\right),$$
(18)

where n^- and n^+ are the number of anions and cations, with the mass ionic concentration $n_0$and e the electronic charge respectively. Implicit in the analysis is the assumption that the electrical double layer (EDL) is less than half the plate width, so the potential distribution inside the fluid

medium can be carefully represented by a linearized Poisson-Boltzmann distribution. Introducing the Boltzmann ionic number concentration as:

$$n^{\pm} = e^{\mp\bar{\Phi}} = e^{\mp\frac{ez\bar{\Phi}}{k_B T_v}},$$

(19)

Invoking Eqn. (19) in Eq. (18), we obtain:

$$\frac{\partial\bar{\Phi}}{\partial\bar{Y}} = \kappa^2 \sinh\left(\bar{\Phi}\right).$$

(20)

By minimizing the small zeta potentials, as per the normal practice in electro-osmotic dynamics, the Poisson-Boltzmann distribution can be linearized as the electrical potential produced by most ionic solutions falls within the range of less than or equal to 25mV. Therefore $\sinh\left(\bar{\Phi}\right) \approx \bar{\Phi}$ and Eqn. (17) reduces to:

$$\frac{\partial\bar{\Phi}}{\partial\bar{Y}} = \kappa^2\bar{\Phi},$$

(21)

This is subject to imposition of the boundary conditions $\bar{\Phi} = \xi$ at $\bar{Y} = 0$ and $\bar{\Phi} \to 0$ at $\bar{Y} \to \infty$.

In Eqn. (21) $\kappa = \dfrac{v_{bf}ez}{U_0}\sqrt{\dfrac{2n_0}{\varepsilon_{eff}K_B T_v}} = \dfrac{\left(v_{bf}/U_0\right)}{\lambda_d}$, represents the electro-osmotic parameter or reciprocal of the characteristic thickness of the electrical double layer (EDL).

2.5. Boundary conditions and non-dimensional analysis

The boundary conditions for the flow domain are given by:

$$\begin{aligned}
&\bar{t} \leq 0: \bar{U} = 0, \bar{T} = T_{\infty} \quad \text{for all } \bar{Y} \geq 0, \\
&\bar{t} > 0: \bar{U} = U_0\cos(\tilde{\omega}\bar{t}), \bar{T} = T_w \text{ as } \bar{Y} = 0, \\
&\bar{t} > 0: \bar{U} \to 0, \bar{T} \to T_{\infty} \quad as \ \bar{Y} \to \infty.
\end{aligned}$$

(22)

The following non-dimensional parameters and variables are introduced:

$$y = \frac{\bar{Y} U_0}{\upsilon_{bf}}, \ t = \frac{U_0^2 \bar{t}}{\upsilon_{bf}}, \ u = \frac{\bar{U}}{U_0}, v = \frac{\bar{V}}{U_0}, \ \theta = \frac{\bar{T} - T_\infty}{T_w - T_\infty}, H = \frac{Q_0 \upsilon_{bf}}{U_0^2 \rho_{bf} (c_p)_{bf}}, Uhs = \frac{-\bar{\Phi}_{\bar{X}} \varepsilon_{eff} \xi}{\mu_{bf} U_0},$$

$$\Phi = \frac{\bar{\Phi}}{\xi}, Gr = \frac{g \beta_{bf} \upsilon_{bf} (T_w - T_\infty)}{U_0^3}, \Pr = \frac{\mu_{bf} (c_p)_{bf}}{\kappa_{bf}}, R = \frac{16 \tilde{\sigma} T_\infty^3}{3 \tilde{k} \kappa_{bf}}, \sqrt{Ta} = \frac{\upsilon_{bf} \Omega}{U_0^2}, \omega = \frac{\tilde{\omega} \upsilon_{bf}}{U_0^2}. \tag{23}$$

Implementing Eqn. (23) in the appropriate conservation equations, the following dimensionless transport equations for electrical potential, axial momentum, transverse momentum and energy emerge:

$$\frac{\partial^2 \Phi}{\partial y^2} = \kappa^2 \Phi, \tag{24}$$

$$\frac{\partial u}{\partial t} = a_3 \left(1 + \frac{1}{\gamma}\right) \frac{\partial^2 u}{\partial y^2} + Gra_5 \ \theta + 2\sqrt{Ta} \ v + a_1 Uhs \frac{\partial^2 \Phi}{\partial y^2}, \tag{25}$$

$$\frac{\partial v}{\partial t} = a_3 \left(1 + \frac{1}{\gamma}\right) \frac{\partial^2 v}{\partial y^2} + Gra_5 \ \theta - 2\sqrt{Ta} \ u, \tag{26}$$

$$\frac{\partial \theta}{\partial t} = a_8 \frac{\partial^2 \theta}{\partial y^2} - a_9 \theta. \tag{27}$$

Here $u, v, \theta, Uhs, Gr, Ta, Pr, R, H$ and ϖ represent respectively the dimensionless axial velocity(primary velocity), transverse (secondary velocity), nanofluid temperature, electroosmotic velocity (or Helmholtz-Smoluchowski velocity (HS velocity)), thermal Grashof number, Taylor number, Prandtl number, thermal radiation parameter, heat absorption/generation parameter and frequency parameter. The corresponding boundary conditions become:

$$\left. \begin{array}{l} t \le 0: u = 0, \ \theta = 0 \ \text{ for all } y > 0, \\ t > 0: u = \cos(\omega t), \ \theta = 1 \text{as } y = 0, \\ t > 0: u \to 0, \ \theta \to 0 \ as \ y \to \infty. \\ \Phi = 1 \ at \ y = 0, \ \Phi \to 0 \ y \to \infty \ for \ t > 0 \end{array} \right\} \tag{28}$$

To facilitate analytical solutions, the primary and secondary momenta Eqns. (25) and (26) can be expressed in the form:

$$\frac{\partial F}{\partial t} = a_{11} \frac{\partial^2 F}{\partial y^2} + Gr \ a_5 \ \theta + a_1 \ Uhs \ \kappa^2 \Phi - 2i \sqrt{Ta} \ F. \tag{29}$$

Here $F = u + iv$ is a complex variable and i is an imaginary number.

3. LAPLACE TRANSFORM SOLUTIONS

Exact solutions for axial and transverse velocity components and nanofluid temperature are derived by solving the dimensionless governing equations from (24), (29) and (27) subject to the boundary conditions (28) using Laplace transforms.

The *electrical potential function* is obtained as:

$$\Phi = \exp(-\kappa y), \tag{30}$$

The hybrid nanoparticle *temperature* distribution is computed as:

$$\theta(y,t) = \frac{1}{2}\left[\exp(y\sqrt{a_9 a_{10}})\,erfc(\eta\sqrt{a_{10}} + \sqrt{a_9 t}) + \exp(-y\sqrt{a_9 a_{10}})\,erfc(\eta\sqrt{a_{10}} - \sqrt{a_9 t})\right], \tag{31}$$

The axial and transverse velocities are combined solutions and emerge as:

$$
\begin{aligned}
F(y,t) = {} & \frac{\exp(i\omega t)}{4}\left[\begin{array}{l}\exp\left(y\sqrt{(i\omega + a_{12})a_{13}}\right)erfc\left(\eta\sqrt{a_{13}} + \sqrt{(i\omega + a_{12})t}\right)\\ + \exp\left(-y\sqrt{(i\omega + a_{12})a_{13}}\right)erfc\left(\eta\sqrt{a_{13}} - \sqrt{(i\omega + a_{12})t}\right)\end{array}\right] \\
& + \frac{\exp(-i\omega t)}{4}\left[\begin{array}{l}\exp\left(y\sqrt{(-i\omega + a_{12})a_{13}}\right)erfc\left(\eta\sqrt{a_{13}} + \sqrt{(-i\omega + a_{12})t}\right)\\ + \exp\left(-y\sqrt{(-i\omega + a_{12})a_{13}}\right)erfc\left(\eta\sqrt{a_{13}} - \sqrt{(-i\omega + a_{12})t}\right)\end{array}\right] \\
& - \frac{a_{20}}{2}\left[\exp(y\sqrt{a_{12}a_{13}})\,erfc(\eta\sqrt{a_{13}} + \sqrt{a_{12}t}) + \exp(-y\sqrt{a_{12}a_{13}})\,erfc(\eta\sqrt{a_{13}} - \sqrt{a_{12}t})\right] \\
& + \frac{a_{19}\exp(-a_{18}t)}{2}\left[\begin{array}{l}\exp(y\sqrt{a_{13}(a_{12}-a_{18})})\,erfc(\eta\sqrt{a_{13}} + \sqrt{(a_{12}-a_{18})t})\\ + \exp(-y\sqrt{a_{13}(a_{12}-a_{18})})\,erfc(\eta\sqrt{a_{13}} - \sqrt{(a_{12}-a_{18})t})\end{array}\right] \\
& + \frac{a_{16}\exp(-a_{15}t)}{2}\left[\begin{array}{l}\exp(y\sqrt{a_{13}(a_{12}-a_{15})})\,erfc(\eta\sqrt{a_{13}} + \sqrt{(a_{12}-a_{15})t})\\ + \exp(-y\sqrt{a_{13}(a_{12}-a_{15})})\,erfc(\eta\sqrt{a_{13}} - \sqrt{(a_{12}-a_{15})t})\end{array}\right] \\
& + \frac{a_{16}}{2}\left[\exp(y\sqrt{a_9 a_{10}})\,erfc(\eta\sqrt{a_{10}} + \sqrt{a_9 t}) + \exp(-y\sqrt{a_9 a_{10}})\,erfc(\eta\sqrt{a_{10}} - \sqrt{a_9 t})\right] \\
& - \frac{a_{16}\exp(-a_{15}t)}{2}\left[\begin{array}{l}\exp(y\sqrt{a_{10}(a_9-a_{15})})\,erfc(\eta\sqrt{a_{10}} + \sqrt{(a_9-a_{15})t})\\ + \exp(-y\sqrt{a_{10}(a_9-a_{15})})\,erfc(\eta\sqrt{a_{10}} - \sqrt{(a_9-a_{15})t})\end{array}\right] \\
& + a_{19}\exp(-Ky) - a_{19}\exp(-a_{18}t)\exp(-Ky).
\end{aligned} \tag{32}
$$

3.1 Nusselt Number (Nu)

The local Nusselt number (*Nu*) defines the dimensionless temperature gradient at the plate surface (and furthermore expresses the relative contribution of convection heat transfer to conduction heat transfer) and can be expressed as:

$$Nu = -\left(\frac{\partial \theta}{\partial y}\right)_{y=0}. \tag{33}$$

The final required expression based on the solution in (31) is:

$$Nu = \sqrt{a_9 a_{10}}\,(1 - erfc(\sqrt{a_9 t})) + \frac{\sqrt{a_{10}}}{\sqrt{\pi t}}\exp(-a_9 t). \tag{34}$$

The coefficients appearing in the above Eqns. take the following definitions:

$$a_1 = \frac{1}{\left(\left(1-\phi_{hnf}\right) + \dfrac{\phi_{Ag}\rho_{Ag} + \phi_{MgO}\rho_{MgO}}{\rho_{bf}}\right)}, \tag{35}$$

$$a_2 = \left(1 + 32.795\phi_{hnf} - 7214\phi_{hnf}^2 + 714600\phi_{hnf}^3 - 0.1941\times10^8\,\phi_{hnf}^4\right),\ a_3 = a_1 a_2, \tag{36}$$

$$a_4 = \left(\left(1-\phi_{hnf}\right) + \frac{\phi_{MgO}\left(\rho\beta\right)_{MgO} + \phi_{Ag}\left(\rho\beta\right)_{Ag}}{\left(\rho\beta\right)_{bf}}\right),, \tag{37}$$

$$a_5 = a_1 a_4,\ a_6 = \left(\left(1-\phi_{hnf}\right) + \frac{\phi_{MgO}\left(\rho c_p\right)_{MgO} + \phi_{Ag}\left(\rho c_p\right)_{Ag}}{\left(\rho c_p\right)_{bf}}\right), \tag{38}$$

$$a_7 = \frac{\left(0.1747\times10^5 + \phi_{hnf}\right)}{0.1747\times10^5 - 0.1498\times10^6\,\phi_{hnf} + 0.1117\times10^7\,\phi_{hnf}^2 + 0.1997\times10^8\,\phi_{hnf}^3}, \tag{39}$$

$$a_8 = \frac{a_7 + R}{a_6\,\mathrm{Pr}},\ a_9 = \frac{H}{a_6},$$

$$\eta = \frac{y}{2\sqrt{t}}, a_{10} = \frac{1}{a_8}, a_{11} = a_3\left(1+\frac{1}{\gamma}\right), a_{12} = 2i\sqrt{Ta}, a_{13} = \frac{1}{a_{11}}, a_{14} = \frac{Gr\,a_5}{1-a_{10}a_{11}},$$

$$a_{15} = \frac{a_{10}a_{11}a_9 - a_{12}}{a_{10}a_{11}-1}, a_{16} = \frac{a_{14}}{a_{15}}, a_{17} = a_1\kappa^2 Uhs, a_{18} = a_{12} - a_{11}\kappa^2, a_{19} = \frac{a_{17}}{a_{18}}, a_{20} = a_{16} + a_{19}. \tag{40}$$

4. NUMERICAL RESULTS, VALIDATION AND DISCUSSION

Extensive evaluation of the closed-form solutions for axial and transverse velocity, temperature and Nusselt number has been achieved in MATLAB software. The objective is to scrutinize the impact of various physical parameters on the axial velocity (u), transvers velocity (v), nanoparticle temperature (θ) and Nusselt number (Nu) profiles. The graphical solutions are visualized for both unitary nanofluid (Ag / H$_2$O) and hybrid nanofluid (Ag-MgO / H$_2$O) in **Figs.2-21**. The values of different variables in computations are $\gamma = 0.5; U\mathrm{hs} = 1; \kappa = 0.5; Pr = 0.71; Ta = 1; H = 0.5; Gr = 2; R = 1$ and $\varpi = \pi$. Specifically we study the influence of Casson viscoplastic fluid parameter (non-Newtonian) (γ), electroosmosis parameter (κ), nanoparticle volume fraction of Ag (ϕ_{Ag}), heat absorption coefficient (H), HS velocity (Uhs), Prandtl number (Pr), Taylor number (Ta) and thermal Grashof number (Gr) on transport characteristics. The various special cases of the present model can be analyzed as follows:

(i) viscous hybrid nanofluid when $\gamma \to \infty$,

(ii) viscous Newtonian fluid when $\gamma \to \infty$ and $\phi_{hnf} = 0$,

(iii) Casson fluid when $\phi_{hnf} = 0$ and $\gamma \neq 0$.

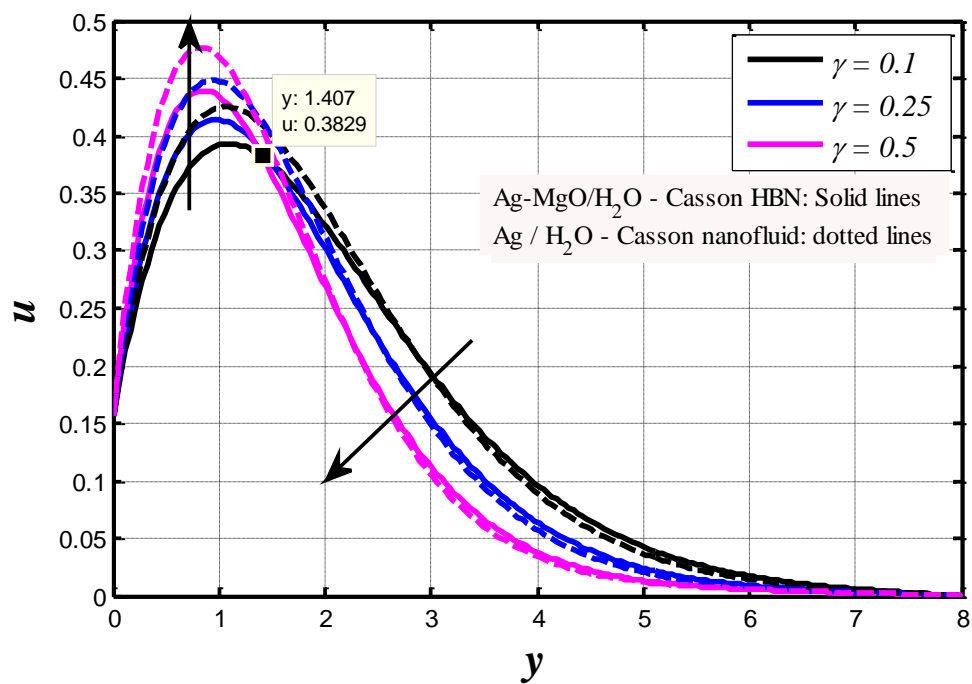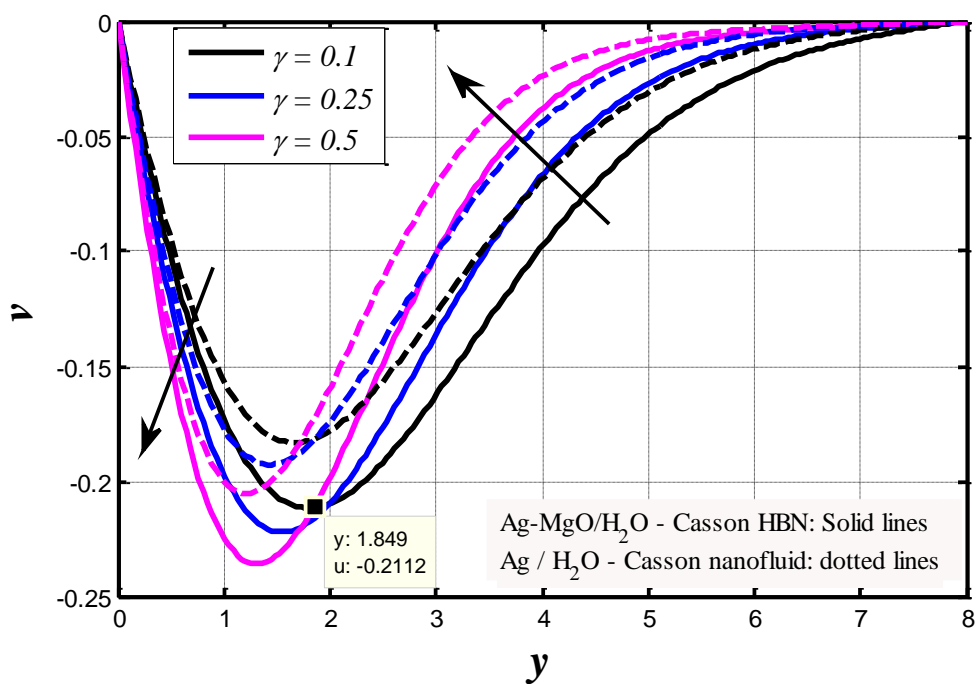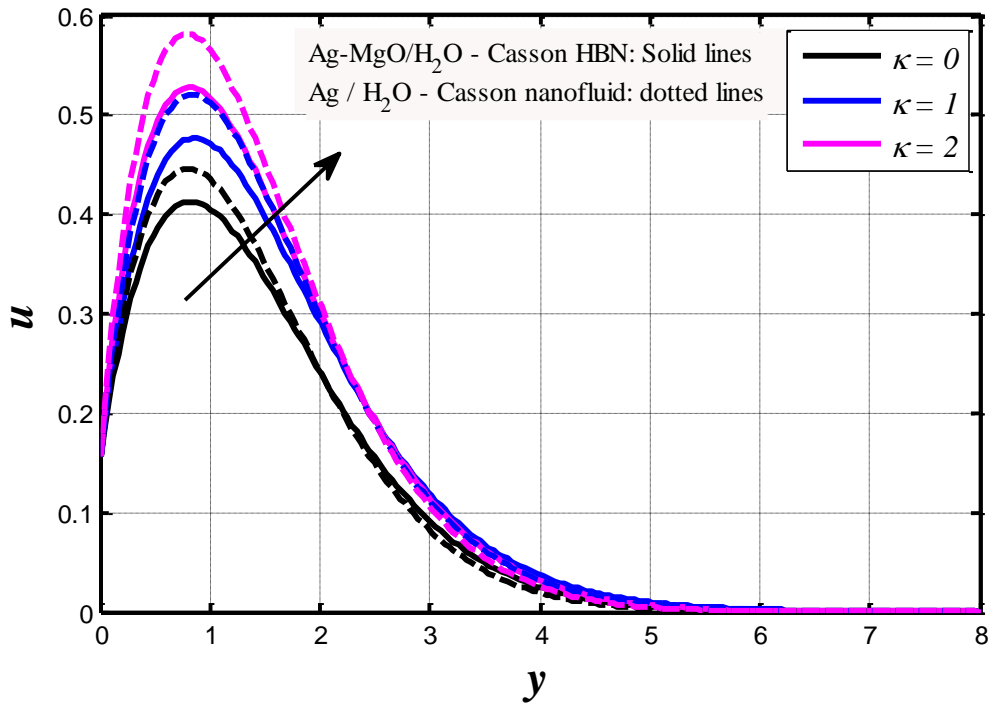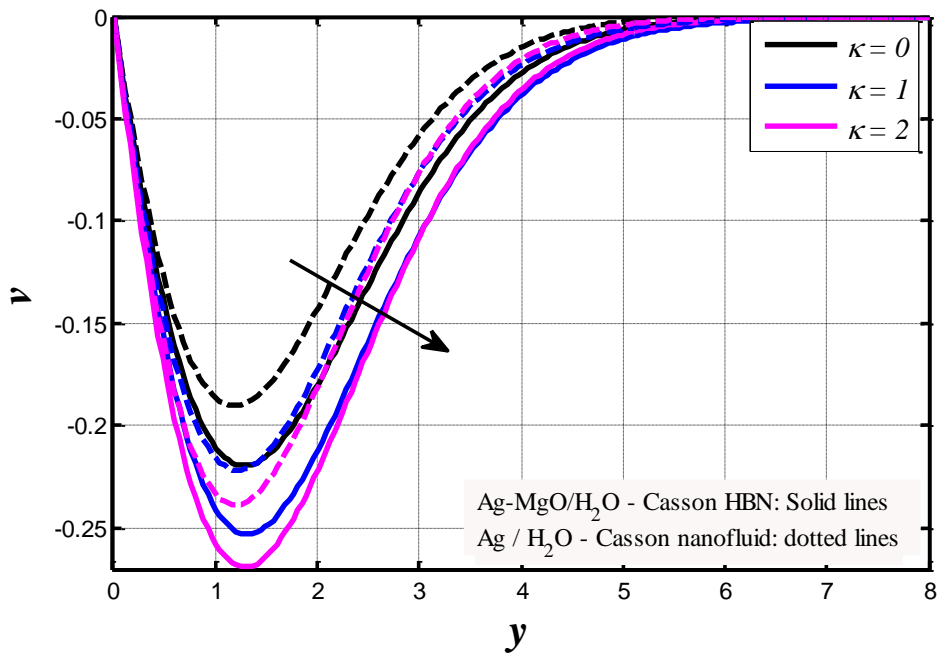**Fig. 2** Effect of γ on axial velocity

Fig. 3 Impact of γ on transverse velocity

Fig. 4 Effect of κ on axial velocity

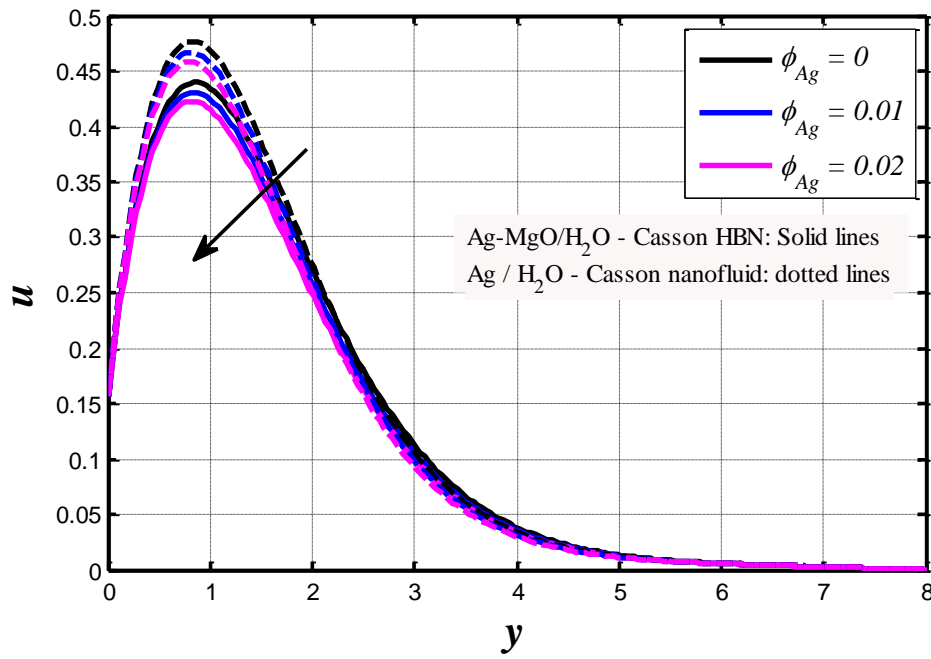**Fig. 5** Impact of κ on transverse velocity

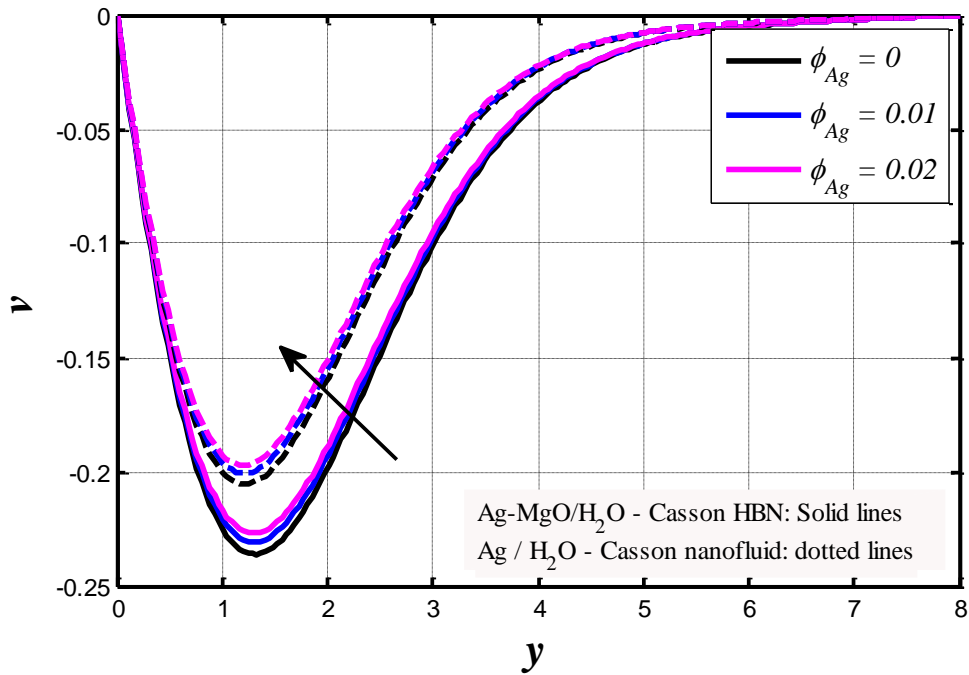**Fig. 6** Effect of ϕ_{Ag} on axial velocity

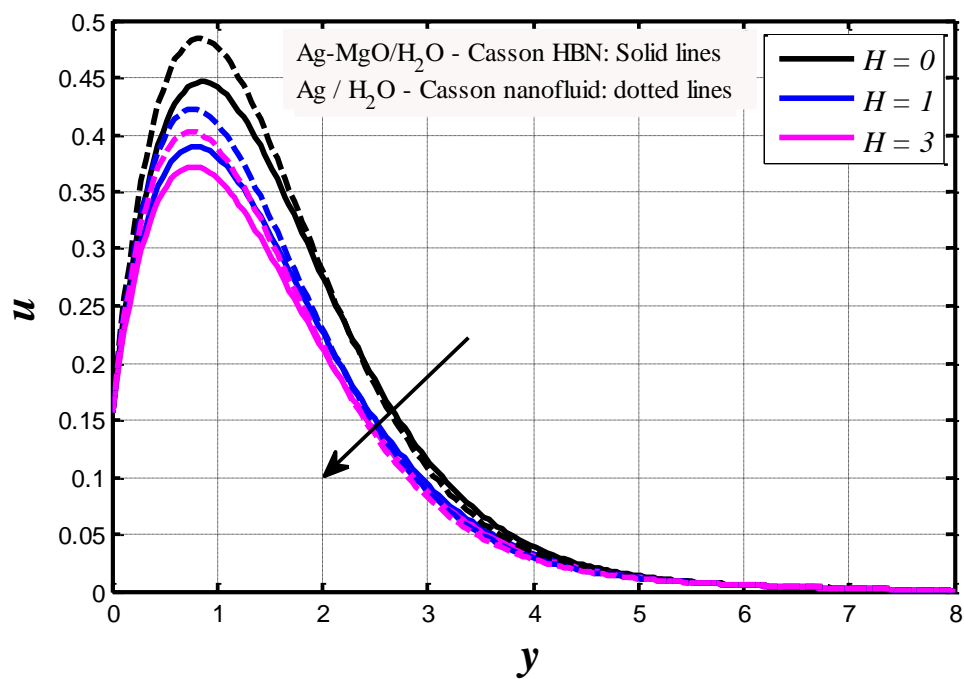**Fig. 7** Impact of ϕ_{Ag} on transverse velocity

20

Fig. 8 Effect of H on axial velocity

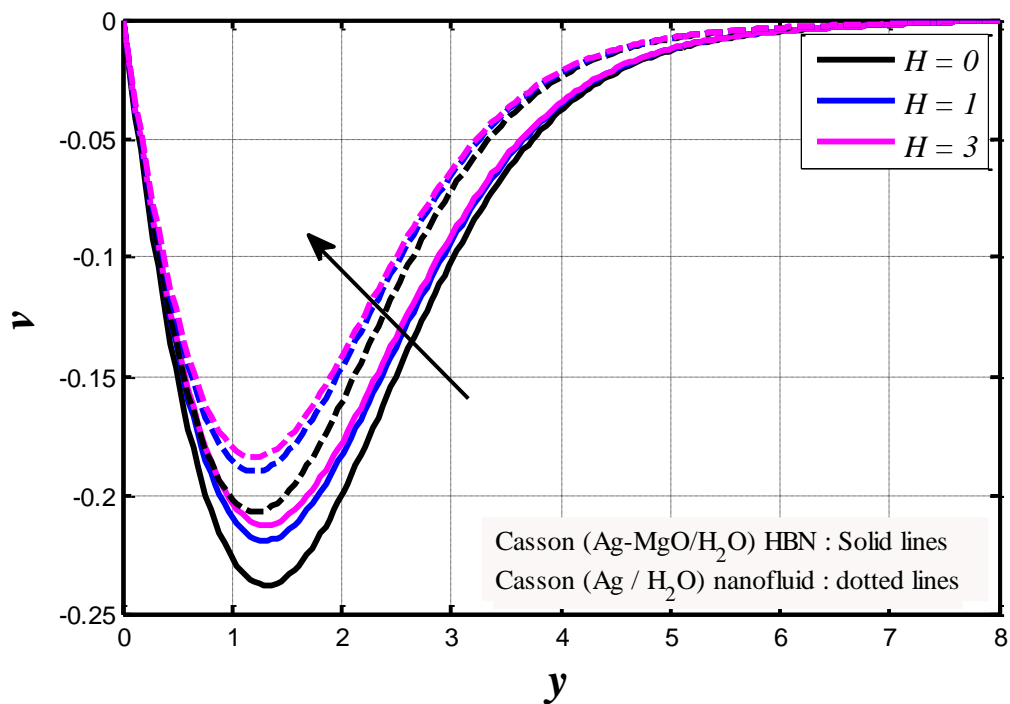**Fig. 9** Impact of H on transverse velocity

Fig. 10 Effect of *Uhs* on axial velocity

Fig. 11 Impact of *Uhs* on transverse velocity
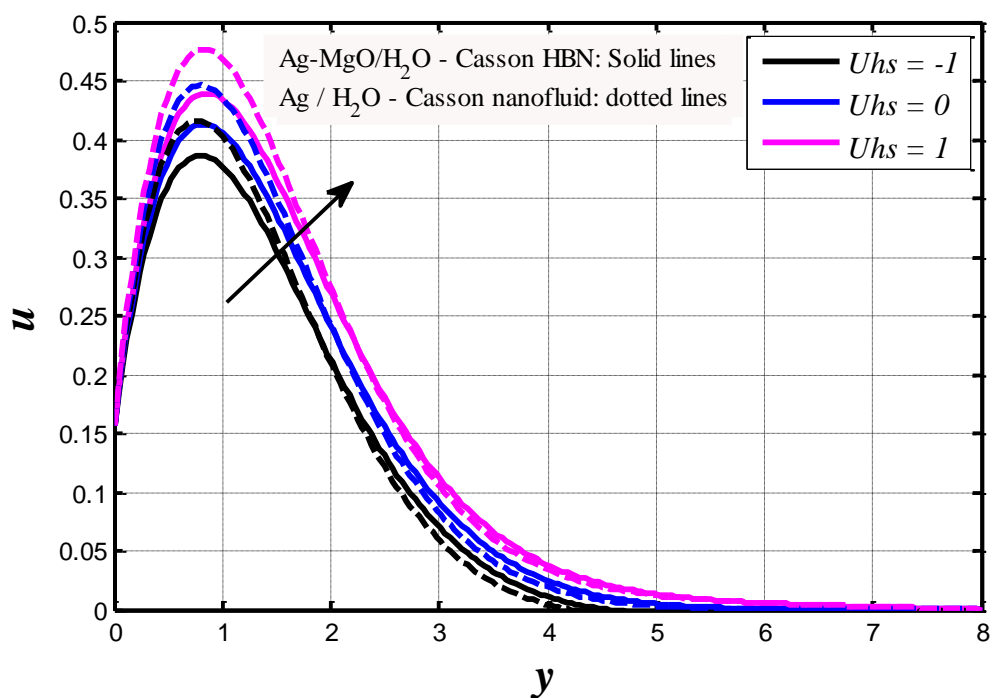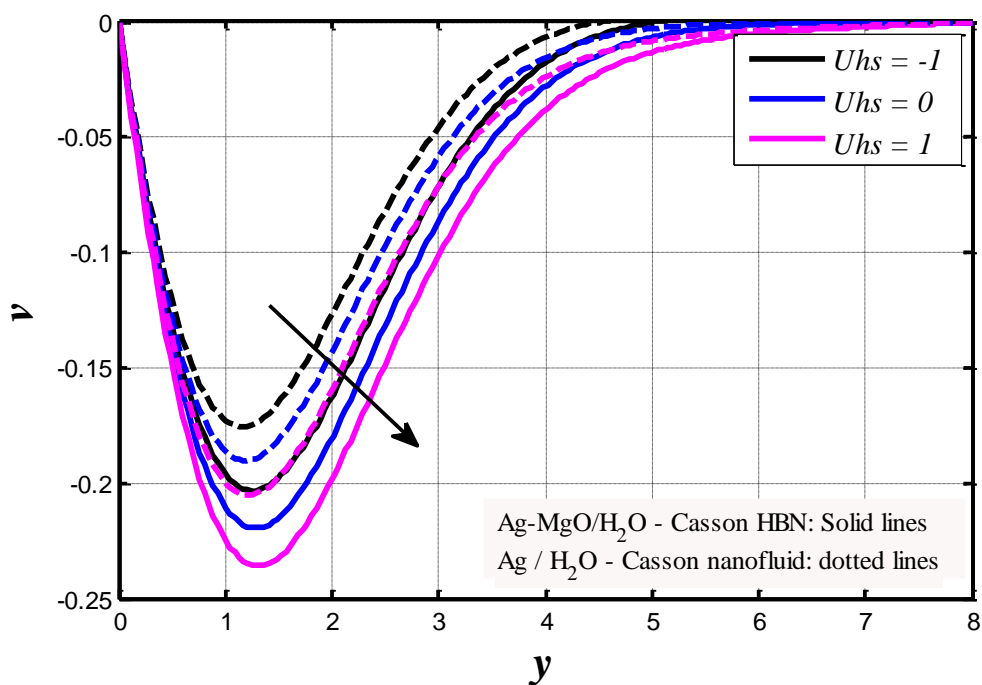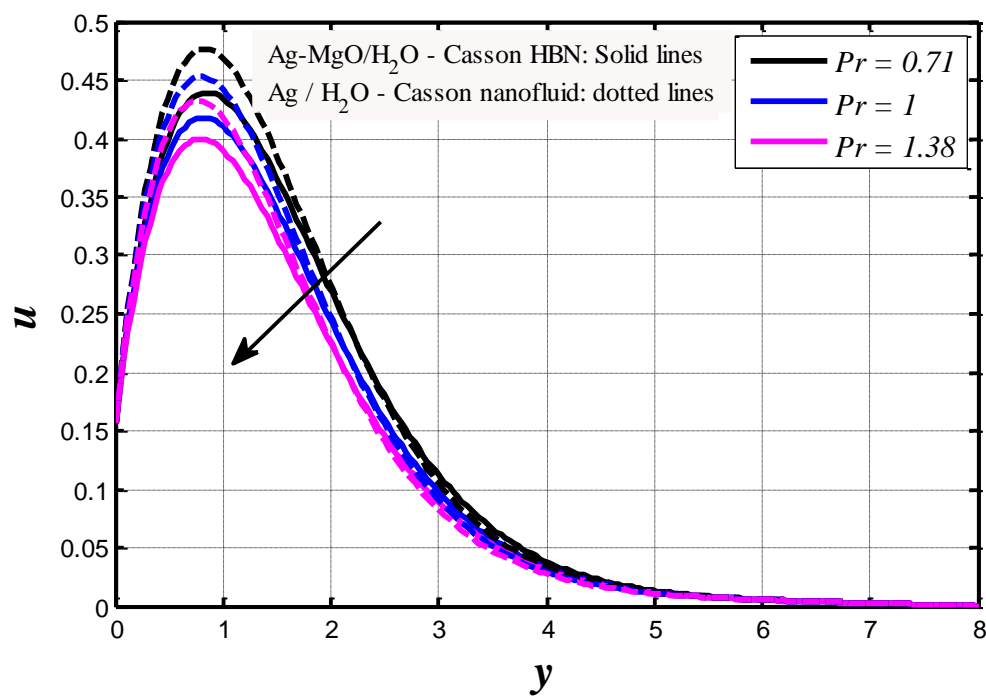
Fig. 12 Effect of Pr on axial velocity
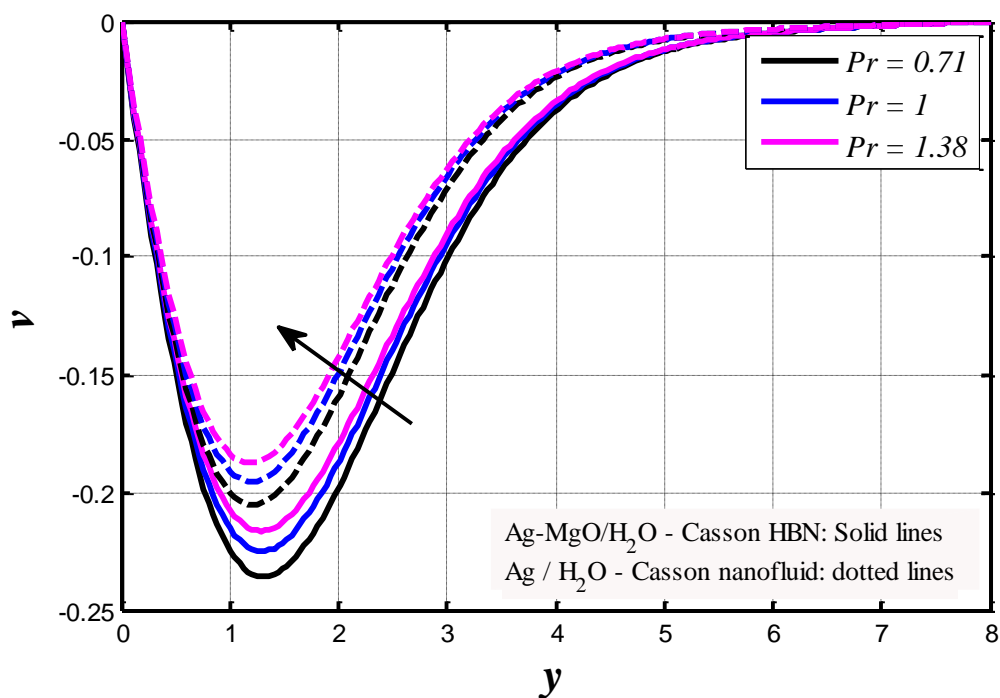
Fig. 13 Impact of Pr on transverse velocity
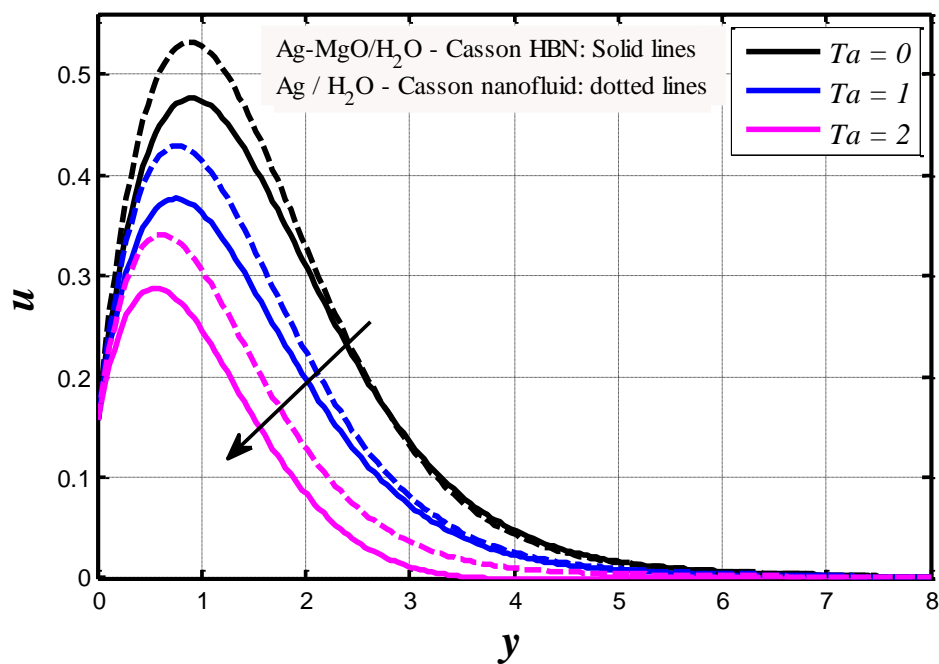
Fig. 14 Effect of Ta on axial velocity
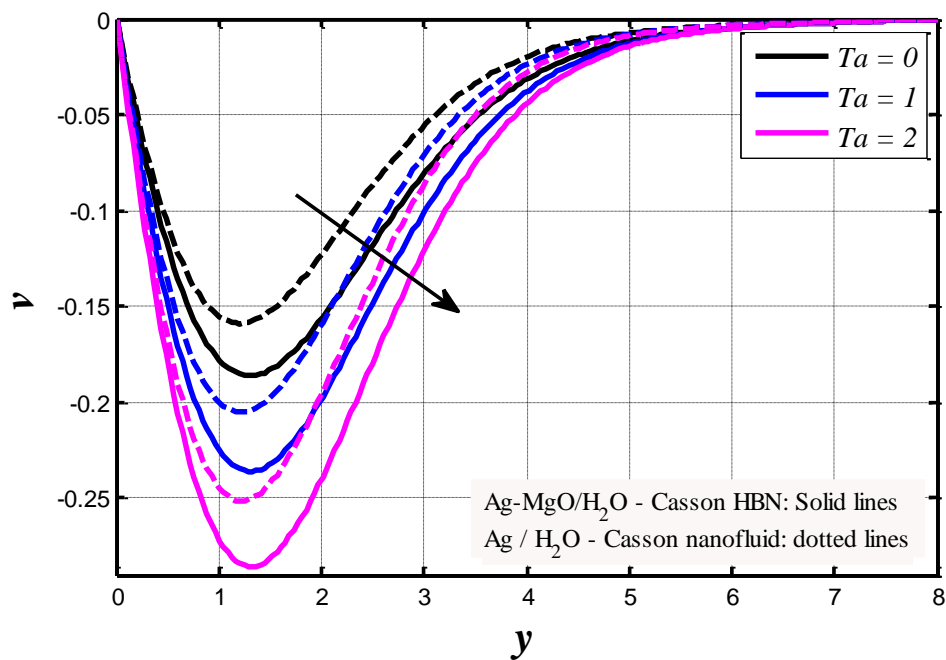
Fig. 15 Impact of Ta on transverse velocity
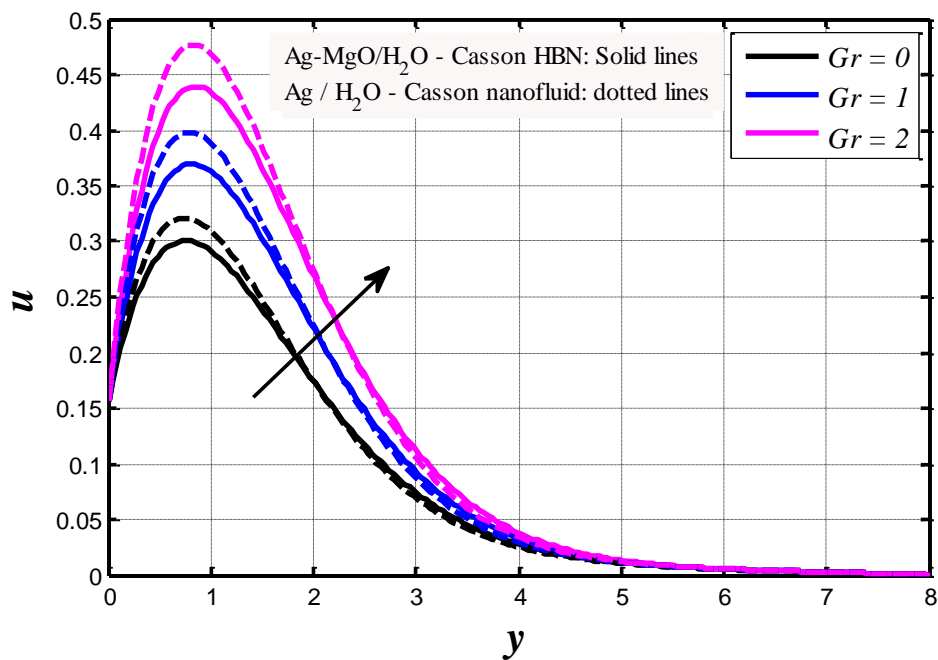
Fig. 16 Effect of *Gr* on axial velocity
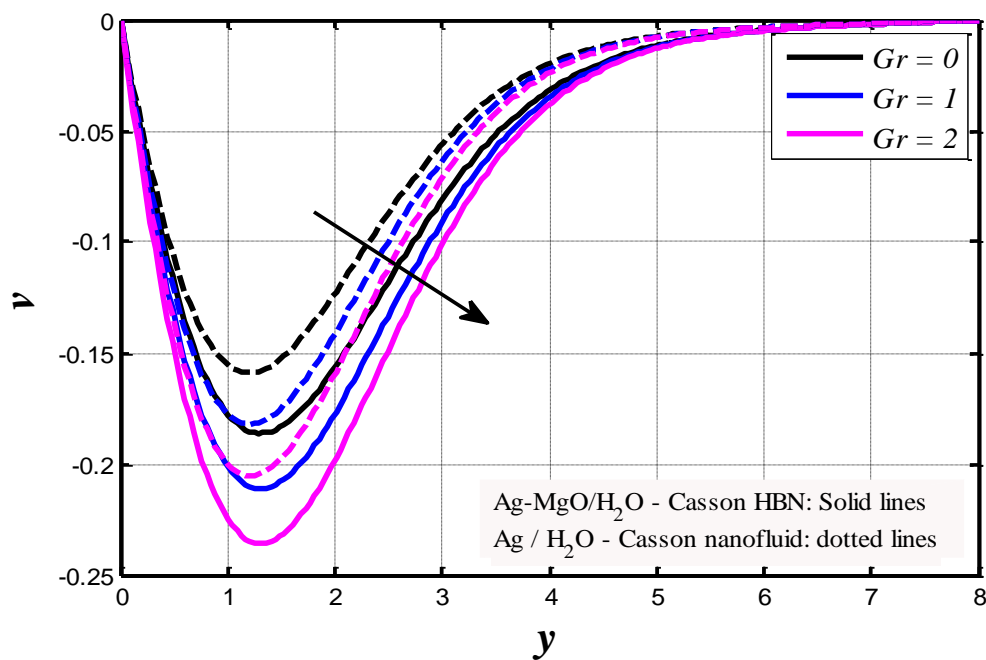
Fig. 17 Impact of *Gr* on transverse velocity
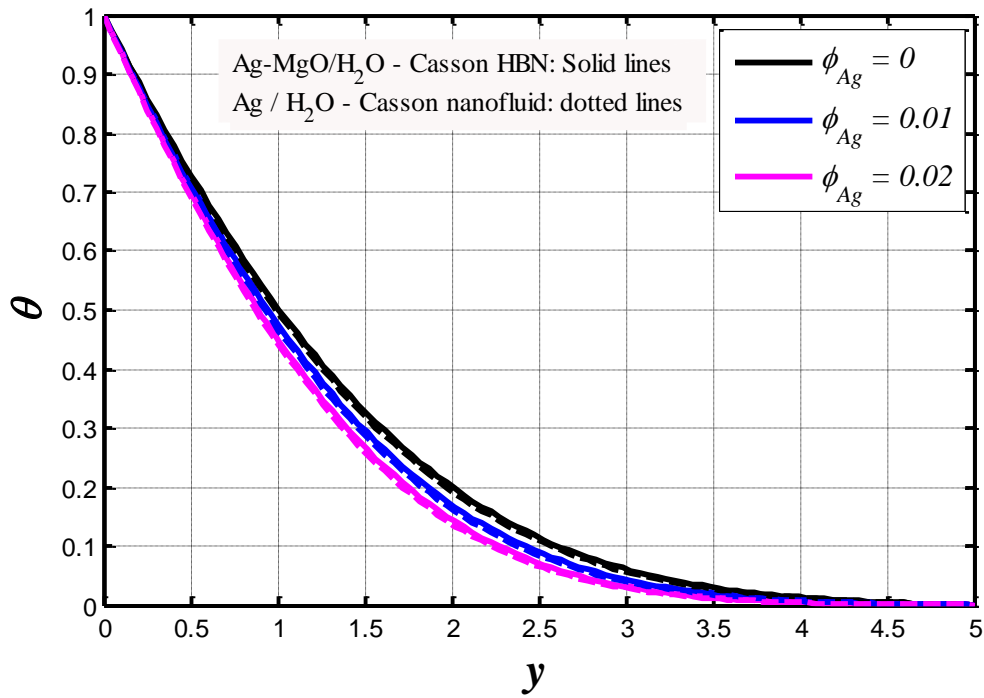
Fig. 18 Analysis of ϕ_{Ag} on nanoparticle temperature distribution
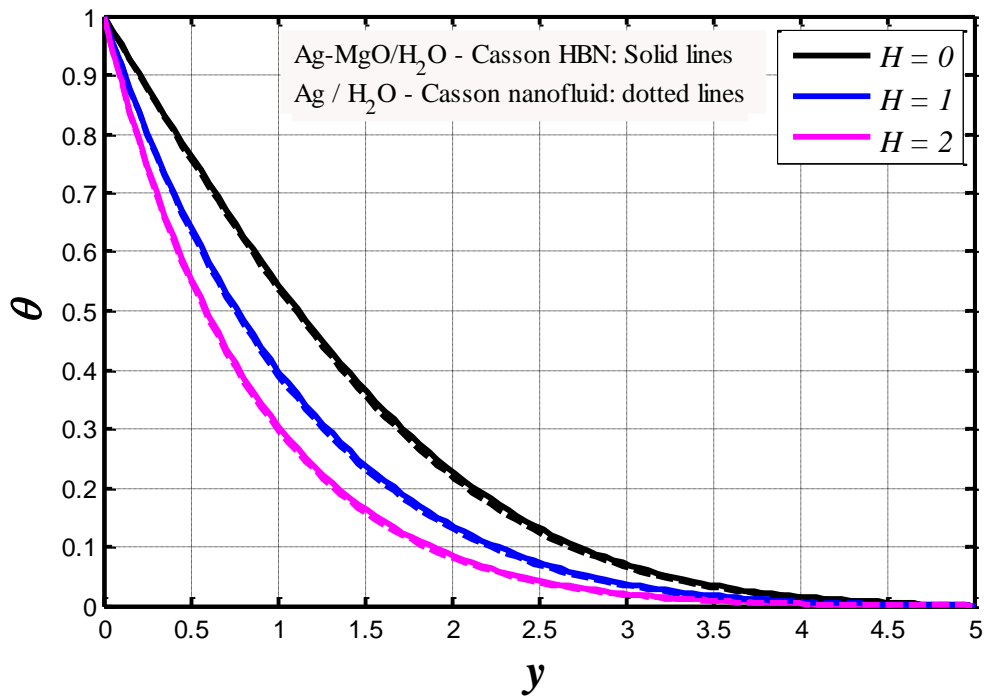
Fig. 19 Analysis of H on nanoparticle temperature distribution

Fig. 20 Analysis of Pr on nanoparticle temperature distribution

Fig. 21 Analysis of R on nanoparticle temperature distribution

Table – 2: Impact of R on Nusselt number, when Pr = 0.71 and H = 0.2

Hybrid nanofluid (Ag-MgO / H_2O)			Unitary nanofluid (Ag / H_2O)		
R/t	0.5	0.7	0.9	R/t	0.5	0.7	0.9
0.5	0.6315	0.4759	0.4138	0.5	0.6668	0.5607	0.4879
1	0.5125	0.4307	0.3745	1	0.5844	0.4914	0.4275
1.5	0.4716	0.3964	0.3447	1.5	0.5265	0.4427	0.3852

Table - 3: Impact of H on Nusselt number, when $Pr = 0.71$ and $R = 0.5$

Hybrid nanofluid (Ag-MgO / H_2O)			Unitary nanofluid (Ag / H_2O)		
H/t	0.5	0.7	0.9	H/t	0.5	0.7	0.9
0.5	0.5354	0.4233	0.346	0.5	0.6317	0.5002	0.4094
1	0.4458	0.3176	0.2338	1	0.5279	0.3771	0.2784
1.5	0.3594	0.2308	0.1532	1.5	0.4271	0.2753	0.1836

Table - 4: Impact of Pr on Nusselt number, when $H = 0.2$ and $R= 0.5$

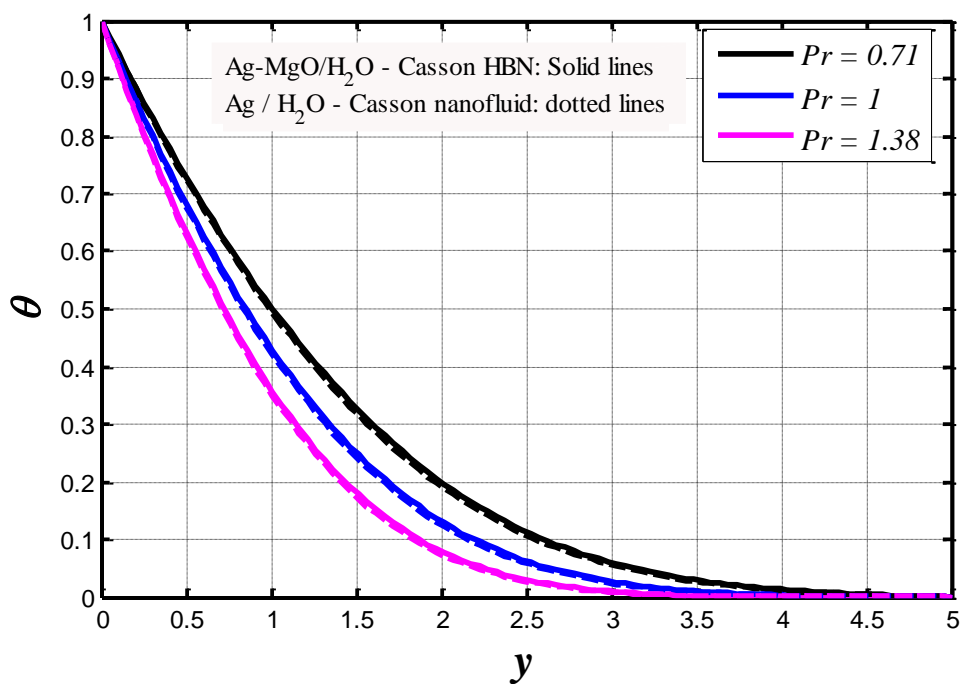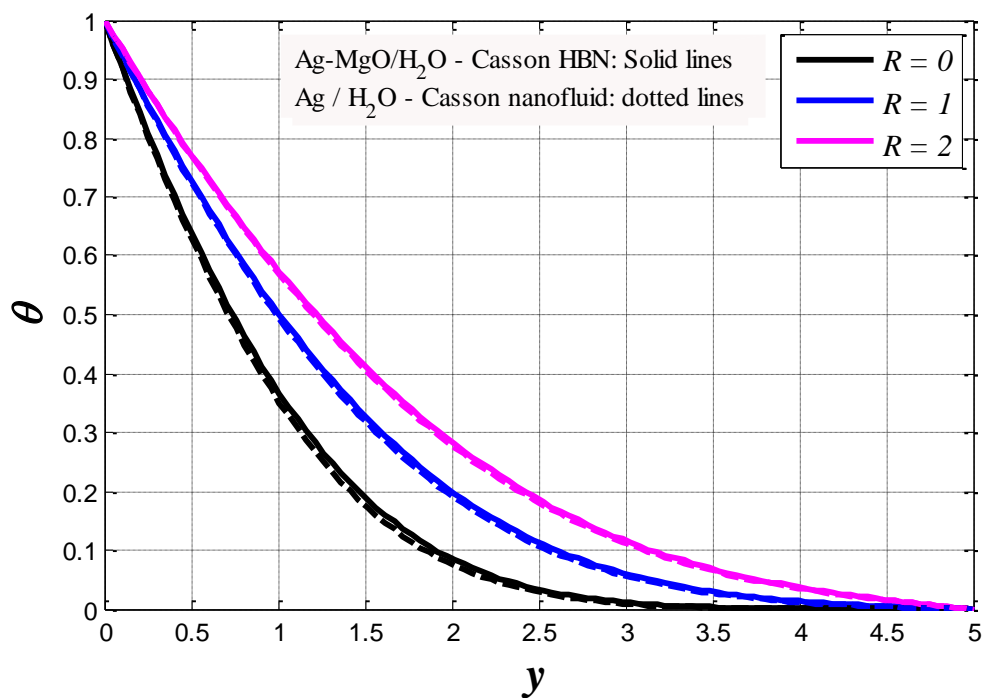| Hybrid nanofluid (Ag-MgO / H_2O)			Unitary nanofluid (Ag / H_2O)		
Pr/t	0.5	0.7	0.9	Pr/t	0.5	0.7	0.9
0.71	0.5662	0.4759	0.4138	0.71	0.6668	0.5607	0.4879
1	0.672	0.5648	0.4911	1	0.7914	0.6655	0.579
7	1.7779	1.4942	1.2994	7	2.0938	1.7606	1.5318

It is noteworthy that in all the plots, the axial (primary) velocity is consistently positive in both cases, and axial flow reversal is never induced. The transverse (secondary) velocity field is generally negative at all locations on the plate surface.

Figs. 2-3 illustrate the impact of Casson viscoplastic fluid parameter on the axial velocity and transverse velocity for both mono (Ag / H_2O) and hybrid nanofluids (Ag-MgO / H_2O). From these figures, it is evident that the axial velocity (Fig. 2) is initially enhanced in the region $0 \leq y \leq 1.407$ and the situation is reversed for the remainder of the region. At the left edge of the plate surface axial velocity is strongly enhanced for (Ag/H_2O) unitary nanofluid relative to the Ag-MgO/H_2O

hybrid nanofluid with increasing Casson parameter; however further along the plate there is greater axial flow acceleration in the latter compared with the former. Further along the plate the axial flow is damped with increasing Casson viscoplastic parameter. The opposite trends are computed for transverse velocity (Fig. 3). Near the left edge of the plate surface transverse i.e. secondary flow is retarded with greater Casson parameter whereas further along the plate it is strongly accelerated. (Ag/H$_2$O) unitary nanofluid achieves slightly higher transverse velocities near the plate compared with Ag-MgO/H$_2$O hybrid nanofluid; however, a much stronger transverse acceleration is computed further along the plate surface.

Figs.4-5 visualize the influence electroosmosis parameter on axial velocity and transverse velocity distributions for both hybrid nanofluid and mono nanofluid. **Fig.4** reveals that the axial velocity is enhanced consistently *at all locations* on the plate surface for both unitary and hybrid nanofluid with greater electroosmotic parameter, κ. However there is a stronger axial flow acceleration computed for the (Ag/H$_2$O) unitary nanofluid relative to the Ag-MgO/H$_2$O hybrid nanofluid. There is a reciprocal relation between the electro-osmotic parameter κ and the characteristic thickness of the electric double layer (EDL) i.e. Debye length parameter, λ_d, as per the relation $\kappa = \frac{v_{bf}\,ez}{U_0}\sqrt{\frac{2n_0}{\varepsilon_{ef}K_BT_v}} = \frac{(v_{bf}/U_0)}{\lambda_d}$. The growth in κ therefore corresponds to a thinner EDL for both hybrid nanofluid and mono nanofluid. For dilute ionic nanofluids (as considered here), the electrical potential increases and generates enhanced mobility of ions. This assists in momentum development and induces primary (axial) flow acceleration. However, in **Fig.5**, increasing κ values manifest in a strong transversal (secondary) flow deceleration i.e. transverse velocity falls (values become more negative) with enhanced values of κ for both cases of mono nanofluid (Ag / H$_2$O) and hybrid nanofluid (Ag-MgO / H$_2$O). The boost in axial momentum is therefore compensated for by a deficit in transverse momentum, in consistency with momentum conservation. Effectively an increase in inverse Debye length (κ) parameter leads to a high primary flow acceleration and a significant secondary flow deceleration, both of which are sustained at all locations on the plate. Engineers may therefore manipulate the intensity of the primary and secondary flow in the rotating ionic nanofluid regime with adjustment in the electro-osmotic parameter.

Figs.6-7 illustrate the evolution in axial and transverse velocities with a change in nanoparticle volume fraction of silver (Ag) for both unitary and hybrid nanofluids. With increasing volume

fraction of silver nanoparticles there is a reduction in axial velocity (flow deceleration) (**Fig. 6**) and elevation in transverse velocity for both nanofluids which is maintained everywhere on the plate. The case of $\phi_{Ag} = 0$ implies zero doping with silver nanoparticles. The nanoparticles are known to move hap hardly via Brownian motion which generally enhances temperatures. Greater concentration of nanoparticles (i.e. higher volume fraction) therefore inhibits momentum diffusion in the axial (primary) flow. When doped with large volume fractions of Ag nanoparticles, the resulting increase in ballistic collisions destroys primary momentum. However the momentum lost in the axial flow is retrieved in the secondary flow (**Fig. 7**) where a substantial acceleration is observed *at all locations on the plate (boundary) surface*. Generally unitary (Ag / H$_2$O) nanofluid produces markedly greater primary (axial) and secondary (transversal) velocity magnitudes relative to hybrid (Ag-MgO / H$_2$O) nanofluid indicating that flow acceleration is best achieved with a single nanoparticle (Ag) in the flow domain.

Figs.8-9 depict the influence of the heat absorption coefficient $\left(H \right)$ on the axial velocity and transverse velocity again for both unitary nanofluid (Ag / H$_2$O) and hybrid nanofluid (Ag-MgO / H$_2$O). The maximum axial velocity (Fig. 8) of unitary nanofluid (Ag / H$_2$O) and hybrid nanofluid (Ag-MgO / H$_2$O) are clearly computed in the absence of heat absorption (*H=0*). Again, the (Ag-MgO / H$_2$O) hybrid nanofluid produces a lower axial velocity than the (Ag / H$_2$O) nanofluid. Elevation in heat absorption parameter generally strongly decreases axial velocity. **Fig. 9** reveals that the secondary flow exhibits the opposite behavior with increasing heat parameter. Transverse flow acceleration is induced with increasing heat absorption/generation parameter. Minimal transverse velocity is therefore observed in the absence of heat absorption/generation effect (*H* = 0). This trend is *sustained everywhere on the plate surface*.

Figs. 10-11 illustrate the evolution in axial (primary) velocity and transverse (secondary) velocity distributions with different values of HS velocity (Helmholtz Smoluchowski velocity *Uhs*). This is an important electro-kinetic parameter which corresponds to the maximal electroosmotic rate in the rotating system. In electroosmosis this parameter enables the mobility of the bulk solution (ionic nanofluid) against a charged solid surface (plate) under the effect of an electric field to be known. As the diffuse coating is a small distance from the surface of the plate, the cations within migrate towards the cathode under the applied voltage along with the surrounding ionic nanofluid.

The H-S velocity parameter, $U\text{hs} = \frac{-E_{\bar{X}}\varepsilon_{eff}\xi}{\mu_{bf}U_0}$. This parameter is *negative* when the electrical field is in the *positive vertical direction* and *positive when the electrical field direction is reversed*. The orientation of the electrical field therefore exerts a profound effect on ion mobility along the accelerated plate. A positive physical increase in *Uhs* means that there is stronger electric field vertically upwards (i.e. in the $\bar{X}$- direction) and a negative increase indicated a stronger electrical field in the downward direction (i.e. in the negative $\bar{X}$- direction). Negative values of H-S velocity therefore decelerate the axial flow whereas positive values accelerate it (**Fig. 10**). This behaviour is consistently observed at all locations on the plate. **Fig. 11** demonstrates that the opposite behaviour occurs for the transversal (secondary) velocity. Negative values of H-S velocity accelerate the transversal flow whereas positive values decelerate it. With vanishing electro-osmotic body force, *Uhs→0 and the profiles naturally fall in between the negative and positive cases for Uhs.* Again unitary (Ag/H$_2$O) nanofluid achieves greater magnitudes of transverse velocity than hybrid (Ag-MgO / H$_2$O) nanofluid.

Figs.12-13 depict the response in axial and transverse velocity profiles with elevation in the Prandtl number again for both unitary nanofluid (Ag / H$_2$O) and hybrid nanofluid (Ag-MgO / H$_2$O). **Fig.12** indicates that axial velocity is considerably depleted with increasing Prandtl number (i.e. lower thermal conductivity of the nanofluids) at all locations along the plate surface i.e. values of *y* coordinate. Thermal properties of the nanofluids therefore significant influence the axial velocity distribution. Unitary nanofluid (Ag / H$_2$O) consistently produces greater axial velocity magnitudes than the hybrid nanofluid (Ag-MgO / H$_2$O). The axial velocity is therefore maximized with low Prandtl number and minimized with high Prandtl number. **Fig.13** reveals that transverse velocity rises with Prandtl number. Again higher magnitudes of transverse velocity are computed with unitary nanofluid (Ag / H$_2$O) relative to hybrid nanofluid (Ag-MgO / H$_2$O).

Figs. 14-15 depict the impact of the Taylor number, Ta, on axial velocity and transverse velocity again for both the unitary nanofluid (Ag / H$_2$O) and hybrid nanofluid (Ag-MgO / H$_2$O). The Taylor number, $\sqrt{Ta} = \frac{v_{bf}\Omega}{U_0^2}$, represents the ratio of *Coriolis (rotational)* and *viscous hydrodynamic* force in the rotating regime, based on the initial velocity of the exponentially vertical accelerated plate. As the Taylor number increases, the Coriolis force is boosted, which inhibits the axial momentum development. This impedes the axial flow at all locations along the plate. Axial velocity is

therefore a *maximum* for the case where rotation vanishes i.e. ($Ta \rightarrow 0$). Axial velocity is however minimized for maximum Taylor number ($Ta = 2$) for which the Coriolis force is double the hydrodynamic viscous force in the regime. As observed in earlier plots, the unitary nanofluid (Ag / H_2O) consistently attains greater axial velocity magnitudes than the hybrid nanofluid (Ag-MgO / H_2O). **Fig. 15** shows that increasing Taylor number also induces significant deceleration in the transversal flow i.e. transversal (secondary) velocity magnitudes become increasingly negative with greater Coriolis force effect. Therefore distinct from other parameters considered which induce different behaviour in the primary and secondary flow, the Taylor number consistently retards both axial and transversal velocity and is an excellent damping mechanism in rotating electroosmotic nanofluid systems.

Figs.16- 17 visualize the effect of thermal Grashof number *Gr* on primary (axial) velocity *u* and secondary (transversal) velocity *v* again for both the unitary nanofluid (Ag / H_2O) and hybrid nanofluid (Ag-MgO / H_2O). The Grashof thermal number quantifies the relative contribution of the thermal buoyancy force and viscous hydrodynamic force, as defined by $Gr = \frac{g\beta_{bf}v_{bf}(T_w - T_\infty)}{U_0^3}$ in Eqn. (23). For the *forced convection* case, *Gr* = 0, and axial velocity is minimized. However with rising value of Grashof thermal number there is a substantial boost in axial velocity everywhere along the plate. Greater axial velocity corresponds to the unitary nanofluid (Ag / H_2O) than the hybrid nanofluid (Ag-MgO / H_2O) (Fig.16). Thermal buoyancy clearly accentuates the electro-osmotic axial flow since more intense convection currents energize the system and counteract gravity effects leading to axial flow acceleration. **Fig. 17** shows that transverse (secondary) velocity exhibits a very different response with modification in Grashof number. Transverse velocity is usually negative and with increasing Grashof number it is further reduced, i.e. stronger thermal buoyancy force strongly damps the secondary (transversal) flow at all locations along the plate length (y coordinate). The hybrid nanofluid (Ag-MgO / H_2O) however produces lower transversal velocity than the unitary nanofluid (Ag / H_2O) since the latter exhibits a less negative velocity. It is reported that a rise in the thermal Grashof number or any other buoyancy-related parameter suggests an increase in the wall temperature, which weakens the fluid-fluid bond, reduces the strength of internal friction, and makes gravity stronger. i.e., causes a significant difference in specific weight between the fluid layers immediately near to the wall. In the flow analysis, a boundary layer is created on the surface and the effects of the buoyancy

parameter are quite important. This is only possible when the specified surface temperature and wall heat flow are taken into account.

Figs. 18-21 illustrate respectively the impact of *Ag* nanoparticle volume fraction (Fig.18), heat absorption coefficient (*H*) (Fig.19), Prandtl number (Fig.20) and thermal radiation parameter (Fig.21) on the temperature distribution (θ) along the plate length (i.e. versus *y*-coordinate). Again we consider both cases of unitary nanofluid (Ag / H$_2$O) and hybrid nanofluid (Ag-MgO / H$_2$O). It is noticed that generally the nanoparticle temperature of unitary nanofluid (Ag / H$_2$O) is *slightly lower* than the hybrid nanofluid (Ag-MgO / H$_2$O) and this is attributable to the overall marginally higher thermal conductivity of combined silver and magnesium oxide nanoparticles compared with unitary silver nanoparticles (Fig.18). With increasing *Ag* nanoparticle volume fraction, temperature of both nanofluids is reduced. **Fig. 19** shows that the overall temperature of the nanofluid is reduced with increasing heat absorption effect since heat is removed from the regime. A *significant reduction* in temperature of both unitary nanofluid (Ag / H$_2$O) and hybrid nanofluid (Ag-MgO / H$_2$O) is observed with increment in Prandtl number (**Fig.20).** The thermal conductivity is suppressed with greater Prandtl number and this suppresses thermal diffusion in the regime. A cooling effect is therefore produced with higher Prandtl number. **Fig.21**displays the evolution in temperature with increment in thermal radiation parameter values (*R*). $R = \frac{16\tilde{\sigma}T_\infty^3}{3\tilde{k}\kappa_{bf}}$ and quantifies the relative contribution of thermal radiative flux to conductive flux. When $R = 1$ both heat transfer modes contribute equally. For $R = 0$ radiative flux vanishes. When $R< 1$ thermal conduction dominates whereas when $R> 1$ thermal radiation dominates. Both unitary and hybrid nanofluid temperatures are minimum when $R = 0$. However with increasing R, there is intensification in radiative flux which energizes the regime and elevates temperatures. The thermal conduction is augmented with greater radiative heat transfer and thermal diffusion in the nanofluid is encouraged.

Tables 2-4 document the values of Nusselt number (*Nu*) with selected parameters (*R*, *Pr*, *H*) and dimensionless time parameter (*t*) for both unitary nanofluid (Ag / H$_2$O) and hybrid nanofluid (Ag-MgO / H$_2$O). Nusselt number calculates the thermal gradient at the plane surface and also measures the relative contribution of convection heat transfer to conduction heat transfer. **Table 2** shows that *with increasing R and t values* (i.e. greater radiative flux and progression in time) there is a

substantial decrease in Nusselt number for both nanofluids. However unitary nanofluid achieves higher Nusselt numbers than hybrid nanofluid. The reduction in Nusselt number with greater radiative effect is explained by the fact that temperatures are increased with greater radiative effect implying that effectively greater heat transport away *from the plate surface to the nanofluid* is produced i.e. heat transfer *to the plate* is suppressed leading to a depletion in Nusselt numbers. Similarly **Table 3** shows that with increasing heat absorption/generation parameter, H and time, t, there is also a consistent decrease in Nusselt numbers. **Table 4** indicates that with increasing Prandtl number there is a significant enhancement in Nusselt number whereas with greater ease in time the Nusselt number is reduced, again for both unitary and hybrid nanofluids. The depression in temperatures with greater Prandtl number computed in earlier graphs implies that heat is convected away from the nanofluid to the wall (plate). This results in an elevation in Nusselt numbers. Overall irrespective of the parameter being varied, there is a consistent suppression in Nusselt number with progression in time.

The numerical results for the fluid velocity at $\gamma = 1$, $Ta = 0$, $Uhs = 0$, $\phi_{hnf} = 0$ and $t = 1$ for the present model and the solutions of Das *et al.* [64] model are documented in Table-5. Absolute errors between both the results are calculated to examine the correlation between both the results. Table-5 reveals that excellent correlation is obtained and thereby the present solutions are validated.

Table – 5: Fluid velocity in the absence of M, Gr, Gm, ϖ for fixed values $\gamma = 1$, $Ta = 0$, $Uhs = 0$, $\phi_{hnf} = 0$, $t = 1$, compared with results of Das *et al.* [64]

y	Fluid velocity (u) Present Model	Fluid velocity (u) Das *et al*. [64] Model	Absolute Error
0.0	1.00000	1.00000	0.00000
0.3	0.88066	0.88063	0.00003
0.6	0.76399	0.76393	0.00006
0.9	0.65247	0.65239	0.00008
1.2	0.54827	0.54817	0.00010
1.5	0.45307	0.45296	0.00011
1.8	0.36804	0.36792	0.00012
2.1	0.29377	0.29365	0.00012
2.4	0.23033	0.23022	0.00012
2.7	0.17735	0.17724	0.00011
3.0	0.13406	0.13396	0.00010
3.3	0.09947	0.09939	0.00008
3.6	0.07242	0.07235	0.00007
3.9	0.05172	0.05166	0.00006
4.2	0.03620	0.03616	0.00005
4.5	0.02478	0.02475	0.00003
4.8	0.01651	0.01648	0.00003
5.1	0.01054	0.01053	0.00002
5.4	0.00619	0.00618	0.00001
5.7	0.00285	0.00285	0.00000
6.0	0.00010	0.00010	0.00000

5. CONCLUDING REMARKS

A rotating Casson hybrid (and unitary) nanofluid electro-osmotic flow model over vertical accelerated plate in the presence of thermal radiation, heat absorption and buoyancy forces is presented. Unitary nanofluid (Ag / H_2O) and hybrid nanofluid (Ag-MgO / H_2O) are considered with an empirical relation employed to calculate thermal conductivities. The dimensionless linearized conservation equations have been derived using Laplace transforms with appropriate boundary conditions. Numerical evaluation and graphical depiction of the impact of key parameters on the transport characteristics (axial velocity, transverse velocity, temperature and Nusselt number) have been conducted with MATLAB software. Both cases of upward and downward electrical field have been studied via an appropriate Helmholtz- Smoluchowski velocity parameter. The computations have shown that:

1) With increasing volume fraction of *silver nanoparticles* there is a reduction in both axial velocity and temperatures whereas there is a distinct elevation in transverse velocity for both unitary and hybrid nanofluids.

2) Elevation in heat absorption parameter strongly decreases axial velocity whereas it boosts transverse velocity.

3) Increasing radiation parameter strongly boosts temperatures. Increasing heat absorption parameter significantly accelerates the transverse flow.

4) Negative values of Helmholtz-Smoluchowski velocity decelerate the axial flow (primary) whereas positive values accelerate it; the opposite behavior is observed for transverse (secondary) velocity.

5) Increasing Taylor number significantly damps the axial flow and transverse flow

6) Increasing thermal Grashof number strongly enhances the axial flow but damps the transverse flow.

7) With increasing Casson viscoplastic non-Newtonian parameter, axial velocity profile is initially increased on the plate surface but further along the plate axial flow deceleration is induced. The contrary behaviour is computed for the transverse velocity for both unitary nanofluid (Ag / H_2O) and hybrid nanofluid (Ag-MgO / H_2O).

8) Unitary nanofluid achieves higher Nusselt numbers than hybrid nanofluid but these are decreased with greater radiative effect (since greater heat transport away from the plate surface), Prandtl number and heat absorption.

9) Nusselt number is significantly reduced with greater time progression and values are consistently higher for unitary nanofluid compared with hybrid nanofluid.

In this work some interesting characteristics associated with rotating non-Newtonian (viscoplastic) electro-osmotic nanofluid flow and heat transfer have been identified. Future studies may generalize the analysis to examine more complex rheological models e.g. viscoelastic and address different metallic/metallic oxide nanoparticle combinations e.g. titania, alumina, copper oxide, silver oxide.

NOMENCLATURE

$P_{\bar{Y}}$	yield stress of the viscoplastic nanofluid
$\left(\bar{U}, \bar{V}\right)$	dimensional velocity components (ms^{-1}) in axial and transverse direction of $\left(\bar{X}, \bar{Y}\right)$
g	acceleration due to gravity (m s^{-2})
Q_0	variable volumetric rate of heat source/sink (kg m^{-1}s^{-3})
$\bar{q}_r$	radiative heat flux (kg s^{-3})
$\tilde{k}$	mean absorption coefficient (m^{-1})
$\bar{T}$	dimensional temperature (K)
$\bar{t}$	dimensional time (s)
t	dimensionless time
z	valence
$\left(n^-, n^+\right)$	number of anions and cations
n_0	mass ionic concentration
e	electronic charge $(\mathrm{kg}^{1/2}\mathrm{m}\Omega^{-1/2}\sec^{-1/2})$
K_B	Boltzmann constant $(\mathrm{kgm}^2\sec^{-2}\mathrm{Kelvin}^{-1})$
T_v	mean temperature (K)
T_w	temperature of the plate (K)
T_∞	temperature of the fluid far away from the plate(K)
$\left(u, v\right)$	dimensionless component of axial and transverse velocities of (x, y) direction
Uhs	electroosmotic velocity or Helmholtz-Smoluchowski velocity (HS velocity)
Gr	thermal Grashof number
Ta	Taylor number
Pr	Prandtl number
R	thermal radiation parameter

H	heat absorption/generation parameter
Nu	Nusselt number

Greek symbols

$\bar{\Phi}_{\bar{X}}$	electric forces
$\bar{\Phi}$	electric potential
π	production of the rate of deformation variable itself
π_c	critical value in Casson viscoplastic model
γ	Casson viscoplastic parameter
ρ_{hnf}	density of hybrid nanofluid (kg m^{-3})
μ_{hnf}	plastic dynamic viscosity (kg m^{-1}s^{-1})
Ω	angular velocity of the plate (rad/s)
$(\rho\beta)_{hnf}$	thermal expansion coefficient of hybird nanofluid ($kgm^{-3}K^{-1}$)
$(\rho c_p)_{hnf}$	heat capacitance of the hybrid nanofluid ($K^{-1}s^{-2}kg\,m^{-1}$)
κ_{hnf}	thermal conductivity of hybrid nanofluid ($Wm^{-1}K^{-1}$)
κ	electro-osmotic parameter
ρ_e	net charge number density
$\tilde{\sigma}$	Stefan-Boltzmann constant $(Kg\,s^{-3}K^{-4})$
$\tilde{k}$	mean absorption coefficient (m^{-1})
ε_{eff}	relative permittivity of the vacuum $(A^2m^{-3}\,s^4\,kg^{-1}=m^{-1}\,s\,(\Omega hm)^{-1})$
ϕ_{hnf}	hybrid nanoparticle volume fraction of silver (Ag) and magnesium oxide (MgO) suspended in water (H_2O)
ϕ_{Ag}	silver nanoparticles
ϕ_{MgO}	magnesium oxide nanoparticles
θ	nanoparticle temperature,
$\bar{\omega}$	dimensional frequency parameter
ω	dimensionless frequency parameter

Subscripts

bf	base fluid
Ag	sliver
MgO	magnesium oxide

REFERENCES

1. Stokes GG. On the effect of the internal friction of fluids on the motion of pendulums. *Transactions of the Cambridge Philosophical Society Part II*. 1851; 9: 8-106.

2. Pohlhausen E. Der Wärmeaustausch zwischen festen Körpern und Flüssigkeiten mitkleiner Reibung und kleiner Wärmeleitung. *Z.A.M.M.*, 1921; 1: pp. 115-121.

3. Schuh, H., 'Einige Problem ebeifreier Stromungzaher', Flussigkeliten (1946, unpublished) see also Gottinger Monographien 1946, Vol. B, Grenzschichten.

4. Schmidt E, Beckmann W. Das temperatur-und Geschwindig-keitsfieldvoreiner Warmeabgeben den senkrechten Platte beinaturlicherkonvektion. Tech. Mech.u. Thermo dynamic . 1930; 341-391.

5. Ostrach S. Analysis of laminar free convection flow and heat transfer about flat plate parallel to direction of generating body force. *NACN TN IIII*; 1953.

6. Soundalgekar VM. Free convection effects on the Stokes' problem for an infinite vertical plate. *ASME. J. Heat Transfer*. 1977; 99: 499.

7. Yang, JW, Scaccia C, and Goodman J. (1974). Laminar natural convection about vertical plates with oscillatory surface temperature. *ASME. J. Heat Transfer*.1974. 96:9.

8. Akbar NS, Tripathi D, Khanand Z, Anwar Bég O. A numerical study of magnetohydrodynamic transport of nanofluids from a vertical stretching sheet with exponential temperature-dependent viscosity and buoyancy effects. *Chemical Physics Letters*. 2016; 661: 20-30.

9. Amanulla CH, Nagendra N, Subba Rao A, Anwar Bég O, Kadir A. Numerical exploration of thermal radiation and Biot number effects on the flow of a non-Newtonian MHD Williamson fluid over a vertical convective surface, *Heat Transfer-Asian Research.* 2017; (19 pages).   DOI: 10.1002/htj.21299

10. Janardhana Reddy G, Kumar M and Anwar Bég O. Effect of temperature dependent viscosity on entropy generation in transient viscoelastic polymeric fluid flow from an isothermal vertical plate. *Physica A - Statistical Mechanics and its Applications*. 2018; 510; 426–445.

11. Hiremath A, Janardhana Reddy G, Mahesh Kumar, Anwar Bég O. Unsteady free convective heat transfer in third-grade fluid flow from an isothermal vertical plate: a thermodynamic analysis. Int. J. Modern Physics B. 2019; 33: 1950060.1- 1950060.36.

12. Ramachandra Prasad V, Vasu B, Anwar Bég O. Thermo-diffusion and diffusion-thermo effects on MHD free convection flow past a vertical porous plate embedded in a non-Darcian porous medium. *Chemical Engineering Journal*. 2011; 173:598– 606.

13. Sadaf, Hina, and Sara I. Abdelsalam. "Adverse effects of a hybrid nanofluid in a wavy non-uniform annulus with convective boundary conditions." *RSC Advances* 10, no. 26 (2020): 15035-15043.

14. Riaz, Arshad, Muhammad Mubashir Bhatti, Rahmat Ellahi, Ahmed Zeeshan, and Sadiq M Sait. "Mathematical analysis on an asymmetrical wavy motion of blood under the influence entropy generation with convective boundary conditions." *Symmetry* 12, no. 1 (2020): 102.

15. Ali, R., A. Farooq, A. Shahzad, A. C. Benim, A. Iqbal, and M. Razzaq. "Computational approach on three-dimensional flow of couple-stress fluid with convective boundary conditions." *Physica A: Statistical Mechanics and its Applications* 553 (2020): 124056.

16. Khan, M. Waleed Ahmad, M. Ijaz Khan, Tasawar Hayat, and Ahmed Alsaedi. "Numerical solution of MHD flow of power law fluid subject to convective boundary conditions and entropy generation." *Computer Methods and Programs in Biomedicine* 188 (2020): 105262.

17. Das SK. Nanofluids: *Science and Technology*. CRC Press Florida ; 2007.

18. Li H, Ha CS, Kim I. Fabrication of carbon nanotube /SiO2 and carbon nanotube/ SiO2/Ag nanoparticles hybrids by using plasma treatment. Nanoscale Res Lett 2009; 4: 1384–8.

19. Guo S, Dong S, Wang E. Gold/platinum hybrid nanoparticles supported on multi walled carbon nanotube/silica coaxial nanocables: preparation and application as electrocatalysts for oxygen reduction. *J Phys Chem C*. 2008; 112: 2389–93.

20. Jana S, Khojin AS, Zhong WH. Enhancement of fluid thermal conductivity by the addition of single and hybrid nano - additives. *Thermo chim Acta.* 2007; 462: 45–55.

21. Turcu R, Darabont A, Nan A, Aldea N, Macovei D, Bica D, Vekas L, Pana O, Soran ML, Koos AA. et al. New polypyrrole-multiwall carbon nanotubes hybrid materials. *J. Optoelectron. Adv. Mater*. 2006; 8: 643–647.

22. Sarkar J, Ghosh P, Adil A. A review on hybrid nanofluids: Recent research, development and applications. Renew. Sustain. *Energy Rev*. 2015; 43: 164–177.

23. Hemmat Esfe M, Alirezaie A, Rejvani M. An applicable study on the thermal conductivity of SWCNT-MgO hybrid nanofluid and price-performance analysis for energy management. *Appl. Therm. Eng*. 2017; 111 : 1202–1210.

24. Baghbanzadeha M, Rashidib A, Rashtchiana D, Lotfib R, Amrollahib A. Synthesis of spherical silica/multiwall carbon nanotubes hybrid nanostructures and investigation of thermal conductivity of related nanofluids. *Thermo chim Acta*. 2012; 549: 87–94.

25. Devi SPA. Devi SSU. Numerical investigation of hydromagnetichybrid Cu-Al2O3 /water nanofluid flow over a permeable stretching sheet with suction. *Int. J. Nonlinear Sci. Numer. Simul*. 2016;17: 249–257.

26. Devi SSU, Devi SPA. Numerical investigation of three-dimensional hybrid Cu-Al2O3 /water nanofluid flow over a stretching sheet with effecting Lorentz force subject to Newtonian heating. *Can. J. Phys*. 2016; 94 :490–496.

27. Hayat T, Nadeem S. Heat transfer enhancement with Ag-CuO/water hybrid nanofluid. *Results Phys*. 2017; 7: 2317–2324.

28. Lund LA, Omar Z, Raza J, Khan I. Magnetohydrodynamic flow of Cu–Fe3O4/H2O hybrid nanofluid with effect of viscous dissipation: Dual similarity solutions. *J. Therm. Anal. Calorim*. 2020. doi.org/10.1007/s10973-020-09602-1

29. Tripathi J, Vasu B, Anwar Bég O, Reddy Gorla RS. Unsteady hybrid nanoparticle-mediated magneto-hemodynamics and heat transfer through an overlapped stenotic artery: biomedical drug delivery simulation. *Proc. I MechE. Part H - J. Engineering in Medicine*.2020. In press

30. Lund LA, Omar Z, Khan I, Seikh AH, Sherif ESM, Nisar KS, Stability analysis and multiple solution of Cu-Al2O3/H2O nanofluid contains hybrid nanomaterials over a shrinking surface in the presence of viscous dissipation. *J. Mater. Res. Technol*.2020; 9:421–432.

31. Khan MR, Pan K, Khan AU, Nadeem S. Dual solutions for mixed convection flow of SiO2−Al2O3/water hybrid nanofluid near the stagnation point over a curved surface. *Phys. A Stat. Mech. its Appl*. 2020; 547:123959. https://doi.org/10.1016/j.physa.2019.12395.

32. Khan U, Zaib A, Khan I, Baleanu D, Nisar KS. Enhanced heat transfer in moderately ionized liquid due to hybrid MoS2/SiO2 nanofluids exposed by nonlinear radiation: Stability analysis. *Crystals* 2020; 10: 142. https://doi.org/10.3390/cryst10020142.

33. Khashie, NS, Arifin NM, Nazar R, Hafidzuddin EH, Wahi N, Pop I, Magnetohydrodynamics (MHD) axisymmetric flow and heat transfer of a hybrid nanofluid past a radially permeable stretching/shrinking sheet with Joule heating. *Chinese J. Phys*. 64, 251–263 (2020).

34. Hemmat Esfe M, Alirezaie A, Rejvani M. An applicable study on the thermal conductivity of SWCNT-MgO hybrid nanofluid and price-performance analysis for energy management. *Appl. Therm. Eng*.2017; 111: pp. 1202-1210.

35. Ghalambaz M, Sheremet MA, Mehryan SAM, Kashkooli FM, Pop I. Local thermal non-equilibrium analysis of conjugate free convection within a porous enclosure occupied with Ag–MgO hybrid nanofluid. *J. Therm. Anal. Calorim*. 2019; 135: pp. 1381-1398.

36. Sundar LS, Sharma KV, Singh MK, Sousa ACM. Hybrid nanofluids preparation, thermal properties, heat transfer and friction factor – *A review*. *Renew. Sustain. Energy Rev*. 2017; 68: pp. 185-198.

37. Polevoi, VV. Electroosmotic phenomena in plant tissues. Biology Bulletin. 2003; 30 (2): 133–139.

38. Masliyah JH, Bhattacharjee S.   2006.   Electrokinetic   and   Colloid   Transport Phenomena, Wiley, New York, USA.

39. Kherad, MK, Vakili AH, bin Selamat MR. et al. An experimental evaluation of electroosmosis treatment effect on the mechanical and chemical behavior of expansive soils. *Arab J Geosci*. 2020; 13: 260.

40. Chang, H.C.; Yao, L. (2009). Electrokinetically Driven Microfluidics and Nanofluidics, Cambridge University Press, New York (2010).

41. Kaushik P et al., Rotating electroosmotic flow through a polyelectrolyte-grafted microchannel: An analytical solution. *Physics of Fluids*. 2019; 31:022009.

42. Wang SC, Chen HP, Lee CY, Yu CC, Chang HC. AC electro-osmotic mixing induced by non-contact external electrodes. *Biosens Bioelectron*.2006; 22: 263–567.

43. Jian YJ, Liu QS, Yang LG. AC electroosmotic flow of generalized Maxwell fluids in a rectangular micro-channel. *Journal of Non-Newtonian Fluid Mechanics*. 2011; 166:1304–1314 (2011).

44. Ali N, Hussain S, Ullah K, Anwar Bég O, Mathematical modelling of Ellis/Newtonian two-fluid electroosmotic peristaltic pumping in an axisymmetric tube. *European Physical Journal Plus*. 2019; 134: 1-18.

45. Narla VK, Tripathi D, Anwar Bég O. Electroosmosis-modulated viscoelastic embryo transport in uterine hydrodynamics: mathematical modeling. *ASME J. Biomechanical Engineering.* 2019; 141(2): 021003.

46. Tripathi D, Bhushan S, Anwar Bég O. Electro-osmotic flow in a microchannel containing a porous medium with complex wavy walls. *J. Porous Media*. 2020; 23(5): 477–495.

47. Tripathi D, Yadav A, Anwar Bég O. Electro-osmotic flow of couple stress fluids in a micro-channel propagated by peristalsis. *European Physical Journal Plus*.132: 173-185.

48. Zhao C, Yang C. Electro-osmotic mobility of non-Newtonian fluids. *Biomicrofluidics*. 2011; 5: 014110.

49. Lu X, Bose JU, Joo, SW, Qian S, Xuan X, Viscoelastic effects on electrokinetic particle focusing in a constricted microchannel, *Biomicrofluidics*, 9, 014108 (2015).

50. Tripathi D, Sharma A, Anwar Bég O. Electrothermal transport of nanofluids via peristaltic pumping in a finite micro-channel: effects of Joule heating and Helmholtz-Smoluchowski velocity. *Int. J. Heat Mass Transfer*. 2017; 111:138–149.

51. Tripathi D, Sharma A, Anwar Bég O. Joule heating and buoyancy effects in electroosmotic peristaltic transport of nanofluids through a microchannel with complex wave propagation. *Advanced Powder Technology.*29, 639-653 (2018).

52. Prakash J, Tripathi D, Anwar Bég O. Comparative study of hybrid nanofluid performance in microchannel slip flow induced by electroosmosis and peristalsis, *Applied Nanoscience*. 2020: (14 pages). doi.org/10.1007/s13204-020-01286-1

53. Tripathi D, Bhushan S, Anwar Bég O. Transverse magnetic field driven modification in unsteady peristaltic transport with electrical double layer effects, *Colloids and Surfaces A: Physicochemical and Engineering Aspects*. 2016; 506: 32–39.

54. Prakash J, Siva EP, D. Tripathi D, Anwar Bég O. Thermal slip and radiative heat transfer effects on electroosmotic magneto-nanoliquid peristaltic propulsion through a microchannel. *Heat Transfer-Asian Research*. 2019: 27 pages. DOI: 10.1002/htj.21522

55. Li SX, Jian YJ, Xie ZY. Rotating electro-osmotic flow of third grade fluids between two microparallel plates. *Colloids Surface A: Physicochemistry Engineering Aspects*. 2015; 470:240–247.

56. Xie ZY, Jian YJ. Rotating electroosmotic flow of power-law fluids at high zeta potential, *Colloids Surface A: Physicochemistry Engineering Aspects*. 2014; 461:231–239.

57. Meighan MM et al., Bioanalytical separations using electric field gradient techniques. *Electrophoresis*.2009; 30(5):852-65.

58. Hari, R. Kataria, Harshad R Patel. Soret and heat generation effects on MHD Casson fluid flow past an oscillating vertical plate embedded through porous medium. *Alexandria Engineering Journal*.2016; 55: 2125–2137.

59. Esfe MH, Arani AAA, Rezaie M, Yan W-M, Karimipour A. Experimental determination of thermal conductivity and dynamic viscosity of Ag–MgO/water hybrid nanofluid. Int. Comm. *Heat Mass Transfer*. 2015; 66: 189–95.

60. Kalidasan K, Velkennedy R, Kanna PR. Laminar natural convection of Copper–Titania/Water hybrid nanofluid in an open-ended C-shaped enclosure with an isothermal block. *J Mol Liq.* 2017; 246:251–8

61. Kasaeipoor A, Malekshah EH, Kolsi L. Free convection heat transfer and entropy generation analysis of MWCNT-MgO (15%–85%)/water nanofluid using Lattice Boltzmann method in cavity with refrigerant solid body-Experimental thermo-physical properties. *Powder Technol.* 2017; 322: 9–23.

62. Benzema YK, Benkahla N, Labsi SE, Ouyahia M, Ganaoui EI. Second-law analysis of MHD mixed convection heat transfer in a vented irregular cavity filled with Ag-MgO/water hybrid nanofluid. *J. Therm. Anal. Calorim.* 2019; 1-20.

63. Tripathi D, Prakash J, Anwar Bég O and Kumar R. Thermal analysis of γAl2O3/H2O and γAl2O3/C2H6O2elastico-viscous nanofluid flow driven by peristaltic wave propagation with electroosmotic and magnetohydrodynamic effects: applications in nanotechnology energy systems. Energy Systems and Nanotechnology. *Advances in Sustainability Science*

and Technology Book Series, Springer-Nature, Singapore, 2021.doi.org/10.1007/978-981-16-1256-5_13

64. Das M, Mahato R, Nandkeolyar R, Newtonian heating effect on unsteady hydromagnetic Casson fluid flow past a flat plate with heat and mass transfer, *Alexandria Engineering Journal*, 2015; 54: 871–879